Appendix I: eRHIC ERL-Ring Design with Strongly Reduced Risks

Author list: *I. Ben-Zvi, M. Blaskiewicz, S. Brooks, P.Kolb, A. Fedotov, Y. Hao, A. Hershkovitch, H. Huang, Y. Jing, V.N. Litvinenko, C. Liu, Y. Luo, F. Meot, B. Parker, V. Ptitsyn, G. Robert-Demolaize, T. Roser, J. Skaritka, D. Trbojevic, N. Tsoupas, E. Wang, G. Wang, F. Willeke, H. Witte, Q. Wu, C. Xu, W. Xu,*

Acknowledgments to: *E. Aschenauer, W. Fischer, M. Minty, C. Montag, R. Palmer, R. Petty, I. Pinayev, T. Rao, K. Smith, R. Than, J. Tuozzolo, A. Zaltsman*

I.1 The Design Concept

I.1.1 Accelerator Concept, Layout and Major Components

The design described in this Appendix aims to satisfy following requirements defined by eRHIC physics goals:

- CM energy: ~ 20 - 140 GeV
- Luminosity: ~$10^{32\text{-}33}$ cm^{-2} s^{-1}; upgradable to ~$10^{33\text{-}34}$ cm^{-2} s^{-1} with modest facility upgrades depending on R&D progress for ion cooling
- Frequent changes to the spin-sign assignment of the electron and proton beam as determined by the physics requirements
- Beam divergences at the interaction point that do not exceeding the experimental limits

In fulfilling these requirements, the ERL-Ring design option presented here relies as much as possible on the present level of accelerator technology. At the same time a straightforward pass for future luminosity upgrade to 10^{34} cm^{-2}s^{-1} level using a novel cooling technology is provided.

While the main focus of this Low Risk design is on minimizing technological risks, machine construction and operational cost are also important factors to be taken into an account. For the hadron part of the machine, the eRHIC design takes advantage of the existing RHIC accelerator complex, including the full suite of injector systems for polarized protons and fully-stripped heavy ions. The new electron accelerator is achieved through an energy efficient approach by employing the energy recovery technology.

The ERL-Ring design uses one of the RHIC hadron beams (the clockwise-moving “blue” beam), with a high energy electron beam counter-rotating in the same tunnel, and collisions occurring in 1-2 intersection regions occupying the present experimental areas of the STAR (IR6) and PHENIX (IR8) detectors. The full range of RHIC hadron beams is thus available for eRHIC, up to 275 GeV for polarized protons and 110 GeV/u for Au ions.

The electron bunches are generated in a high-current polarized source and are accelerated to 20 MeV in the injector accelerator. They are accelerated in 2 superconducting energy-recovery linacs

(ERLs) thereby gaining up to 3 GeV of energy. Using recirculating loops inside the RHIC tunnel the electrons make multiple passes through the linacs increasing their energy up 3 GeV per turn. A maximum of 18 GeV is reached with six recirculation loops. The electrons can be extracted at any energy from 2 to 18 GeV into a high energy transport beamline which brings them into collision with the hadron beam at either IR6 or IR8. The spent electron bunch is then recirculated back through the linacs, returning its energy to the superconducting RF structure of the linac (energy-recovery process), after which the decelerated electrons are dumped. Thus, each electron bunch participates in only one collision crossing with the hadron beam, and the process repeats itself for each succeeding bunch. The electron bunches are accelerated and brought into collision with the hadron beam at a frequency of 9.4 MHz.

The major eRHIC accelerator components are:

- The 20 MeV injection complex, located at the IR2 area of the RHIC tunnel. It includes a polarized electron source, a bunching system and 20 MeV linear accelerator. The 50 mA current polarized electron source located is based on merging beam currents from multiple electron guns.
- Two 1.5 GeV superconducting Energy Recovery Linacs, located at IR2 and IR10 straight sections. Each ERL is 198 m long and consists of a string of superconducting 647 MHz cavities. The use of energy recovery technology in the main accelerator linac is essential to reach a high value (50mA) of the electron average current. For HOM damping a proven technology using beam pipe absorbers is employed.
- Six vertically stacked recirculation beamlines run around the RHIC tunnel circumference, outside of the hadron ring. One beamline, corresponding to the top energy, runs through the experimental detector(s), while 5 other beamline make bypass around detectors.
- A spreader and a combiner are placed either side of the each ERL for proper distribution and matching of the electron beams of different energies between the ERL and recirculation beamlines. Both the spreader and the combiner have 6 arms used to transport beams of particular energies. The arms also are used for optics matching and path length tuning.
- No proton cooling is needed to achieve the Low Risk design luminosity goals. Present RHIC stochastic cooling system can be efficiently used at e-Au operation.
- The electron-hadron collisions occur in one or two interaction regions (IR6 and IR8 RHIC areas). The interaction regions include superconducting magnets and provide strong focusing to achieve the β^* in 13-26 cm range. The electron and hadron beams are brought into the collision with a 14 mrad crossing angle. Crab cavities are employed to prevent loss of luminosity due to the crossing angle.
- A beam dump for disposing of the decelerated beam is located in IR10 area.

The present RHIC accelerator uses superconducting magnets to circulate hadron beams in two rings of 3834 m circumference. The wide energy reach of RHIC provides a natural opportunity to operate eRHIC over a wide range of center-of-mass collision energies. Existing proven accelerator technologies, exploited in RHIC and its injectors to produce and preserve proton beam polarization, will provide the highly polarized proton beam required for the eRHIC experiments. Modifications of the present RHIC machine for the eRHIC era include new quadrupole and dipole magnets in interaction regions with experimental detectors and additional Siberian Snakes for acceleration of

polarized $^3He^{+2}$. The copper coating of the hadron beam pipe is needed to reduce cryogenic load caused by vacuum pipe heating by the beam.

I.1.2 Design Beam Parameters and Luminosities

Based on the fact that electrons, accelerated by the linear accelerator, collide with the protons (or ions) accelerated and stored in the circular machine, the eRHIC collision scheme is called the "linac-ring" scheme. This scheme has been chosen for eRHIC because of several clear advantages it brings in luminosity and electron polarization. On the luminosity side the "linac-ring" scheme overcomes one of the fundamental luminosity limitations of the "ring-ring" scheme from circulating electron beam quality deterioration caused by many repeating beam-beam interactions. Unlike the electron beam circulating in a storage ring, the electron beam from a linac passes through the collision point(s) only once. Hence, a beam-beam interaction of much higher strength can be allowed, paving the way to higher luminosity. The luminosity of the "linac-ring" scheme can be written as a function of the hadron beam parameters:

$$L = f_c \xi_h \frac{\gamma_h}{\beta_h^*} \frac{ZN_h}{r_h} H_{hg} H_p \ ,$$

where $r_h = Z^2 e^2 / Mc^2$ is the hadron classical radius, ξ_h is the hadron beam-beam parameter, β_h^* is the hadron beta-function at the interaction point, N_h is the hadron bunch intensity, γ_h is the hadron relativistic factor and Z is the hadron charge. f_c is the collision frequency, which is the same as the bunch repetition rate.

The geometric loss factor H_{hg} arises from luminosity loss due to the hour-glass effect and the crossing angle. With a 14 mrad crossing angle at the eRHIC collision points, the crab-crossing technique has to be employed to prevent luminosity loss.

The H_p parameter represents the luminosity enhancement resulting from the pinching of the electron beam size at the collision point caused by the hadron beam focusing force.

The design luminosity and choice of beam parameters are influenced by both physical limits and practical considerations. The major limits assumed for the beam and accelerator parameters are:

- Polarized electron average current: $I_e \leq 50$ mA
- Hadron space-charge tune shift: $\Delta Q_{sp} \leq 0.06$
- Electron synchrotron radiation power: $P_{SR} < 1$ MW

Table I-1 lists the beam parameters and design luminosity for e-p collisions. e-ion collisions have similar luminosity level in terms of electron-nucleon luminosity. The listed values of peak luminosity use the following H-factors: $H_{hg}=0.88$ and $H_p=1.26$. The luminosity reduction by ~8% due to the abort gap is also included.

The eRHIC bunch frequency of 9.4 MHz is equal to the bunch frequency of the present RHIC hadron beam. The proton beam-beam parameter is well below 0.015, a limit observed in RHIC.

Table I-1: Beam parameters for highest luminosity of e-p collisions for LR designs.

	LR Nominal design	
	e	p
Energy [GeV]	13	275
CM energy [GeV]	105	
Bunch frequency [MHz]	9.4	
Bunch intensity [10^{10}]	3.3	30
Beam current [mA]	50	415
rms norm.emittance h/v[um]	64/64	1/1
rms emittance h/v [nm]	2.5/2.5	3.4/3.4
beta*, h/v [cm]	35/17.5	26/13
IP rms beam size h/v [um]	30/21	
IP rms ang. spread h/v [urad]	85/120	115/163
max beam-beam parameter	1.0	0.004
e-beam disruption parameter	6	
max space charge parameter	9e-5	0.004
rms bunch length [cm]	0.3	16
Polarization [%]	80	70
Peak luminosity [$10^{33}cm^{-2}s^{-1}$]	1.2	

I.1.3 Average Luminosity and Store Length

The Low Risk design does not use a proton cooling system. Smallest possible emittances must be produced from the injectors and then preserved during the RHIC energy ramp. Planned studies for achieving minimal emittance are going to address possible effects leading to the emittance growth at the RHIC injection and on the ramp (injection kicker timing, transverse noise, IBS, electron cloud, …) as well as further optimization of scraping technology at the injectors. Longitudinal bunch merging in injectors to get a higher bunch intensity after the scraping is also being considered.

A transverse normalized rms emittance of 1 mm*mrad normalized obtained regularly at the RHIC injection is presently accepted as a baseline emittance for the Low Risk design. Without cooling, the transverse proton beam emittance grows due to intra-beam scattering. With the proton beam-beam parameter as small as 0.004, one does not expect beam loss due to dynamic aperture. Hence, the luminosity evolution in the store is defined by the transverse emittance growth only (Figure I-1, left plot).

Following experience of RHIC runs, the typical turnaround time of about one hour is expected between the stores. Although in best case the turnaround time of 0.5 hours has been demonstrated. The Figure I-1 (right plot) shows that the stores length of 4-6 hours long would be optimal for maximizing average luminosity at the 1h turnaround time.

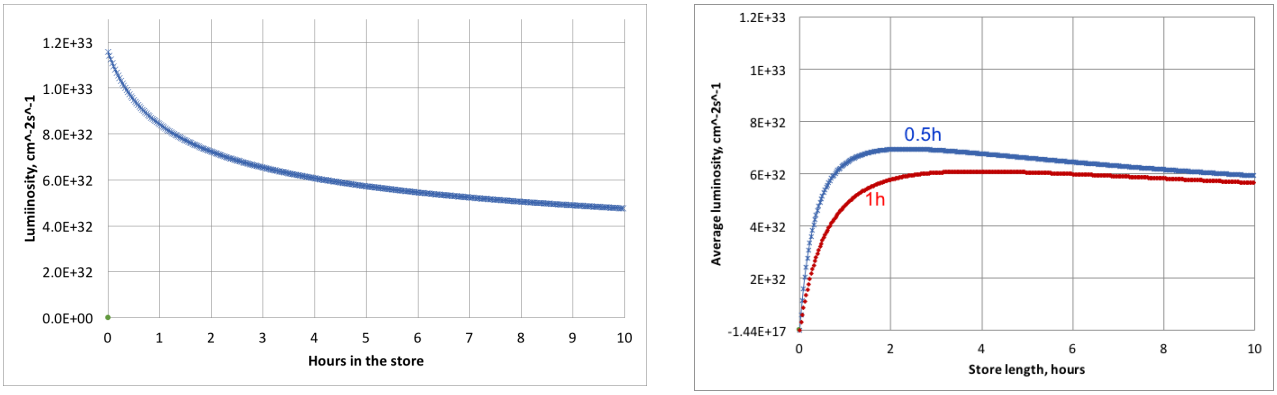

Figure I-1: Left plot: the e-p luminosity evolution in the eRHIC store. Right plot: Average luminosity versus the store length for 0.5h and 1h turnaround time between stores. Both plots are evaluated for the proton beam energy of 275 GeV.

The Figure I-2 shows the dependence of the e-p luminosity on the center-of-mass energy (CME). To maximize the luminosity at various CMEs a preferable way is to vary electron energy at fixed (275 GeV) proton energy. When varying electron energy only, the luminosity remains constant until the synchrotron radiation loss power limit is reached. Accepting the SR loss limit at 1 MW, the luminosity drops at the electron energies above 13 GeV.

At lower CME range one has to vary the proton energy too. The luminosity in this CME area decreases due to increased beam size at the interaction point. For 50 GeV protons the bunch intensity has to be reduced to satisfy the space-charge limit, further decreasing the luminosity.

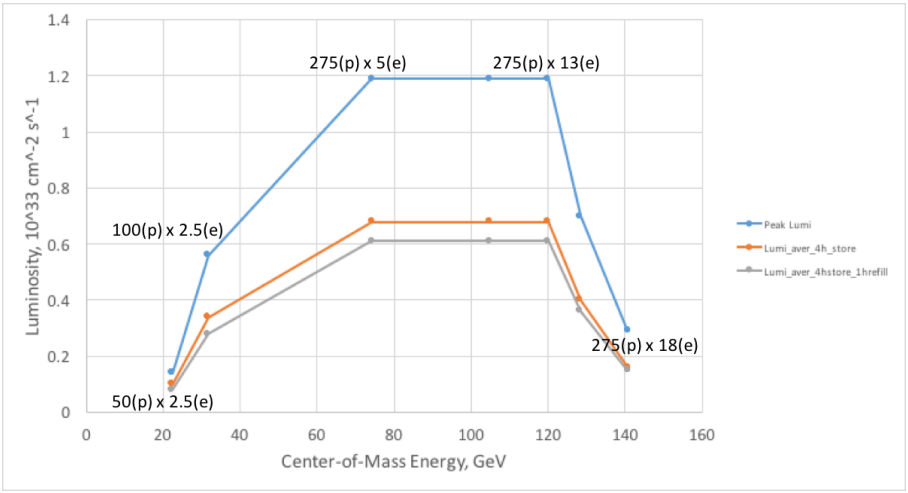

Figure I-2: The e-p luminosity versus center-of-mass energy of e-p collisions. Blue curve: peak luminosity. Orange curve: average luminosity for 4h long store; Grey: average luminosity assuming 4h long stores and 1h turnaround time between the stores.

I.2 Electron Accelerator

I.2.1 Electron Injector and Dump

Polarized electron source

eRHIC will require a highly polarized electron source with high average current, short bunch length and low emittance. The current state-of-the-art polarized electron sources deliver either a high peak current, low average current beam such as the case at SLAC (I_{av} ~0.9 μA, I_{peak}>5A) or a high average current, low peak current beam as produced at JLab (I_{av} = 4 mA, I_{peak}= 53 mA)[1,2,3,4]. eRHIC will require a very high average current (up to 50 mA) with a bunch charge up to 5.3 nC, with moderately low emittance and a long cathode lifetime (at least several hours).

GaAs was selected as a photocathode because it is well established and widely used as a source of highly polarized electrons (P~85-92%) [5]. A current-state-of-the-art single cathode electron source cannot deliver the required 50 mA current with acceptable cathode lifetime due to ion back-bombardment and surface heating induced by very high laser power. But the required current could be achieved by combining electron bunches from multiple guns. The electron source scheme adopted for the ERL-Ring eRHIC uses eight JLab-type inverted DC guns and combines the beams from them into one common line. The JLab gun generated 4mA average current with a laser spot size of 0.3mm on the cathode [4]. This spot size could be increased to 1 mm. Then, each gun of the eRHIC source could generate 6-10 mA. Thus eight guns should be able to generate up to 50 mA average current at sufficiently long cathode lifetime (4-5 hours). The eRHIC guns intend to combine the high bunch charge performance of the SLAC gun with the high average current performance of the JLab gun. Main parameters of an individual electron gun are listed in the Table I-2.

Table I-2: eRHIC polarized gun design parameters.

Cathode material	Distributed Bragg reflector super lattice GaAs*
Cathode size	1.2 cm
Gun voltage	350kV
Laser power	5W~8W
Laser size radius	3.5 mm
Cathode QE	>0.2%
Initial bunch length	1.5ns
Peak current density	9.2A/cm^2
Peak current	3.53A
Average current	6.25mA

In order to combine the beams from individual guns, capacitor-inductance (LC) copper plate RF deflectors are considered as combiner components. These could bend 350keV electron beam by 10 to 30 degrees. The eight-gun combining scheme and the frequency of RF deflectors are shown in Figure I-3.

* Cathode material: Strain-compensated GaAs/GaAsP SL-AlGaAsP/AlAsP DBR-Graded GaAsP with surface p-doping 1.2e^{19}a/c.c from SVT.

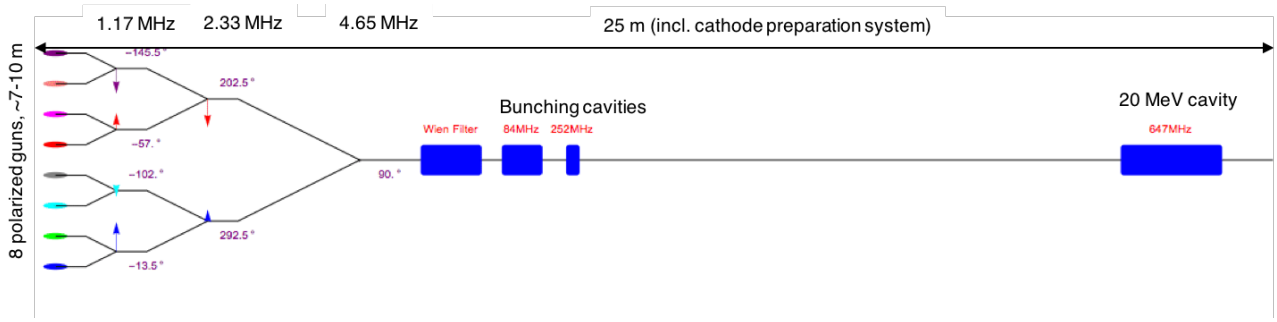

Figure I-3: 20 MeV electron injector including combining scheme for the polarized electron source. The frequencies of the combiners and phases of the RF are listed.

Photocathode preparation

The high current high polarization electron source for eRHIC requires the preparation of GaAs photocathodes. The strained superlattice GaAs activation is a matured technique. Multiple spin electron facilities such as JLab, Mainz, MIT-BATES Nagoya Univ. are such cathode in operation their machines. In BNL, we are able to activate commercial sample to QE above 1% in 780nm. Each of eight guns is accompanied by a preparation chamber. During the preparation in the preparation chamber, the photocathode is heat cleaned up to 580°C for surface cleaning. Once the sample has cooled to the room temperature, a monolayer of Cesium and Oxygen lowers the vacuum level for electrons to come out when the sample is illuminated with laser. This process is known as "Activation" and has to be performed under extreme vacuum conditions (less than 10^{-11} Torr). The BNL activation system is capable to achieve this vacuum regime on a consistent basis. Each cathode preparation, from heat cleaning to activation, takes approximately 4.5 hours. In case of a used GaAs photocathode, re-cesiation could fully recover the cathode QE. This step will take about 20 mins. Superlattice GaAs, which is capable to produce highly polarized electron beam, will be used in the near future to investigate the charge lifetime during multi-cathode operation in the gun. Distributed Bragg Reflector (DBR) GaAs photocathodes were developed and tested in the early 2000s [6]. This could significantly reduce the heat deposition on the cathode and prolong the lifetime, and US industry SVT is capable to grow this type of cathode. In high current operation, we will use DBR GaAs photocathodes in our polarized electron source.

Laser for multiple guns at BNL

In the multiple gun scheme of the eRHIC polarized source each individual gun will have a high-power laser. To produce a highly polarized beam, laser pulses at 780 nm are required to drive photocathode. To realize these pulses Erbium (Er)-doped fiber amplifier (EDFA) laser system at 1560 nm will be built and light at 780 nm will be generated through second harmonic generation (SHG) (Figure I-4). The significant advantages with the fiber laser include high-average output power, diffraction-limited beam profile, low point instability, and maintenance-free operation. In this Er-doped fiber laser system, a master oscillator power amplifier is designed to produce high output. The seed is an active mode-locking fiber laser with 1560 nm central wavelength, 9.38 MHz repetition rate, and 1.5 ns pulse duration. Through an ultrafast switch, optical pulses from the seed are separated into eight pulse trains of 1.17 MHz repetition rate, and fed into eight independent EDFAs for power amplification and frequency doubling. In each EDFA, the laser power will be boosted to 3 W through two preamp stages and 20 W in the main amplifier. A 60 W pump diode at 976 nm and a 30-meter Erbium-doped photonic crystal fiber will be used in the main amplifier. Through SHG, 8 W average power at 780 nm will be produced in each amplifier and used to drive eight DC guns.

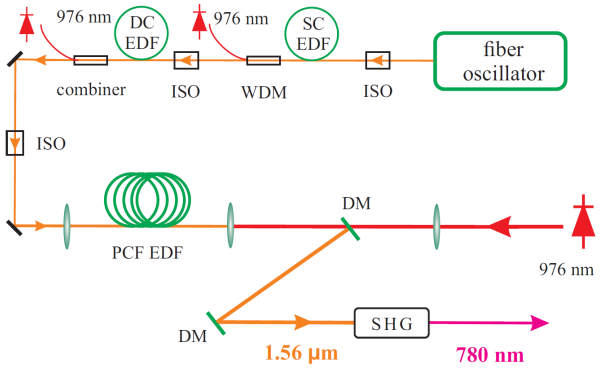

Figure I-4: Schematic of high-power Er-doped fiber amplifier. EDF, Er-doped fiber, SC, single-clad, DC, double-clad, PCF, photonic crystal fiber, SHG, second harmonic generation, IOS, isolator, WDM, wavelength division multiplexing, and DM, dichroic mirror.

e-beam bending in the combiner

The Figure I-5 shows the RF defector electrical field between two copper plates and dog-leg structure of beam bending. The ground plate is placed between two copper plates to enhance the field at beam entrance.

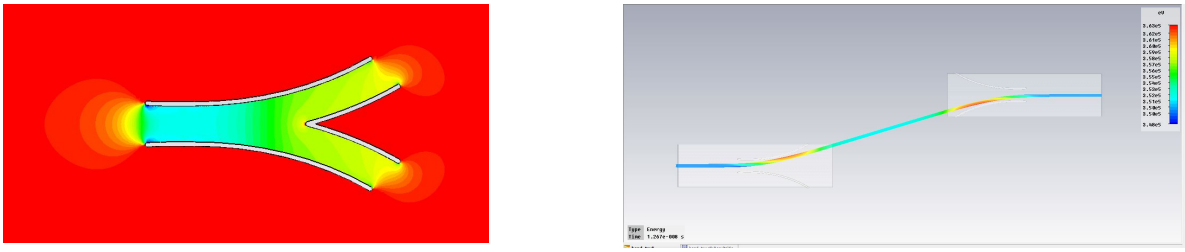

Figure I-5: Left: Field distribution of cooper plate deflector. Right: Dog-leg structure of beam bending and combining.

For example: bending 350 keV beam into 15 degrees, the gradient between the plates is 0.32MV/m. The plate length is 0.46 meters and the plates distance is 7 centimeters. More optimization for the combiner system is ongoing.

We are also studying several alternative beam-combining schemes. The final selection of a combiner must be beneficial both to the gun performance and to achieving eRHIC injector required beam parameters.

The electric field design for beam combination would use resonant circuits which are tuned with a resonating inductor and a pair of tunable external capacitors in parallel with the deflection plates. Having two degrees of freedom in tuning capacitors allows the deflector plate voltages to be balanced with respect to ground in addition to having the network tuned to the precise frequency required.

The frequencies for the three levels of combination are 1.175Mhz, 2.35 MHz, and 4.7MHz. The power amplifiers driving these circuits would range from 150 to 350 Watts. The references to the power amplifiers are derived from scaled phase locked loops comparing the laser timing to the sampled deflector plate voltage. Phase and frequency control of this type is a well-established technology of low level RF.

If a magnetic field design be chosen, it would be an extension of the 650 MHz rotating field combiner developed for the Gatling Gun. In this new design, the dipole field rotational frequency would be 1.175 MHz.

Polarized source operational scenario

There are four GaAs cathodes pre-installed in the preparation chamber of each gun. During initial preparation all four cathodes are heated up to 520 C for surface cleaning. Using large ~1mm diameter emission area on the cathode each gun should be capable to generate 6.25 mA average current at least for 5 hours, providing total of 50 mA average current at the source output. The estimated length of the stores in eRHIC defined by the IBS emittance growth of proton beam is 5 hours, with one-hour turnaround time between stores. In one hour between the stores the cathodes of all 8 guns will be moved out and either re-cesiated or replaced. Here are two possible methods:

1. A used GaAs photocathode could be re-cesiated, typically about 20 mins. Move the cathode in and out take about 30 mins. In 50 mins, the cathode could be retracted, re-cesiated and inserted back.
2. While in beam operation, rest of three cathodes could be re-cesiated. If necessary, could be activated again. In 1 hour operation down time, the used cathode will be replaced by a high QE cathode and insert into the gun. This step takes about 30 mins.

For the method 1, inserted cathode will be promised to have high QE. There is a risk if failure happens in re-cesiation. For method 2, an out-gassing eliminated XHV valve is needed to make sure the stored three cathodes could be survived in valve operation. So far, such valve is not found yet. We will keep investigating free out gassing XHV valve.

Moving cathodes and re-cesiation is done remotely, with no personnel required in the source area. In two weeks, each cathode will be re-cesiated maximum 14 times. On the maintenance day, all used four GaAs cathodes will be replaced to new ones.

Polarized source design studies

Since polarized source presents a highest remaining design risk for the eRHIC Low Risk Linac-Ring option the program of experimental and simulation studies is planned in 2016-2017 to prove critical design features, such us the merging scheme and the gun operation with high bunch charge. The program includes:

- Finalizing the technicalities of the combining scheme
- Detailed 3D simulations of high-charge bunch transport through all injector components
- Experimental studies of single cathode lifetime dependencies (using a Gatling gun prototype)
- Measurements of surface charge limit for SL cathodes using cathode preparation system.

In the course of experimental studies, the hard limit for maximum average current, maximum bunch charge and operation lifetime will be estimated. The study results will help also to optimize the cathode and anode geometry to generate higher bunch charge as well as reduce beam loss.

20 MeV polarized electrons injector

The eRHIC electron injector has to produce up to 50 mA polarized electron beam with longitudinal and transverse beam parameters defined in Table I-3.

Table I-3: eRHIC injector design parameters.

	Parameters for Low Risk design
Energy, MeV	20
Bunch charge, nC	5.3
Bunch frequency, MHz	9.38
Average beam current, mA	50
Min normalized rms transverse emittance, μm	40
Max normalized rms transverse emittance, μm	72
rms bunch length, mm	3
rms energy spread, %	< 1

Due to non-axial-symmetry of the RF deflector, we are using GPT 3D beam tracking code to design the injection beamline. The simulation is being carried out on both NERSC and BNL cluster. Initially, a four-gun scheme is used for checking the beam quality, bunch length and beam envelop.

Figure I-3 presents a layout of the 20 MeV electron injector. It consists of multiple JLab electron guns and combining RF deflector, 84MHz bunching cavities and a 3rd harmonic cavity, a drift space for ballistic bunch compression and a 647 MHz booster linac. Using the Distributed Bragg Reflection super lattice GaAs photocathode, the JLab DC gun is adopted as the electron source for beam optics baseline design. The gun operates at 350kV with the 2.1 MV/m cathode gradient. 1ns bunches are extracted from the gun and combined by the RF combiners. There is a Wien filter placed between combining point and bunching section for fast rotating the electrons spin direction. The injector beam optics are still under development. The scheme may change later to further meet the requirements of eRHIC.

The Low Risk eRHIC design shall present a normalized RMS emittance requirement of 40 mm-mrad for the eRHIC injector. Detailed studies of the factors that affect emittance growth in the gun, e-beam transport and combining methods shall be evaluated through analytical modeling. In the 8 gun deflector concept combining beams of 5.3 nC per bunch with about a 1ns bunch length traveling more than 20 meters while meeting the current emittance requirement will still be challenging because the plate deflectors and Wien filter have non-symmetric fields, Extensive 3D simulation is required for these beam dynamics studies. These simulations are computationally intensive and time consuming given present capabilities. We will acquire additional computing power to make the most efficient use of our present resources to successfully accomplish these studies in time to satisfy programmatic requirements. Using these new tools the gun R&D group shall work closely with the Linac R&D group on beam optic optimization of the Gun design and combiner variants whilst evaluating and refining the low risk e-beam specifications.

The Low Risk eRHIC Design Study presents a normalized RMS emittance requirement of 40 mm-mrad for the eRHIC injector. Detailed studies of the factors that affect emittance growth in the gun, e-beam transport and combining methods shall be evaluated through analytical modeling. In the 8 gun deflector concept combining beams of 5.3nC per bunch with about a 1ns bunch length traveling more than 20 meters while meeting the current emittance requirement will still be challenging because the plate deflectors and Wien filter have non-symmetric fields, Extensive 3D simulation is required for these beam dynamics studies. These simulations are computationally intensive and time consuming given present capabilities. We will acquire additional computing power to make the most efficient use of our present resources to successfully accomplish these studies in time to satisfy programmatic requirements. Using these new tools the beam optic optimization of the Gun design

and combiner variants will be realized whilst evaluating and refining the low risk e-beam specifications. Full simulations are large efforts; at this point we do not see difficulties which could not be overcome.

The Figure I-6 shows the GPT results for initial simulations done for acceleration up to 10 MeV. Using four guns, the RMS normalized transverse emittance could reach to 40 mm-mrad. The bunch length could be compressed to 2.3mm.

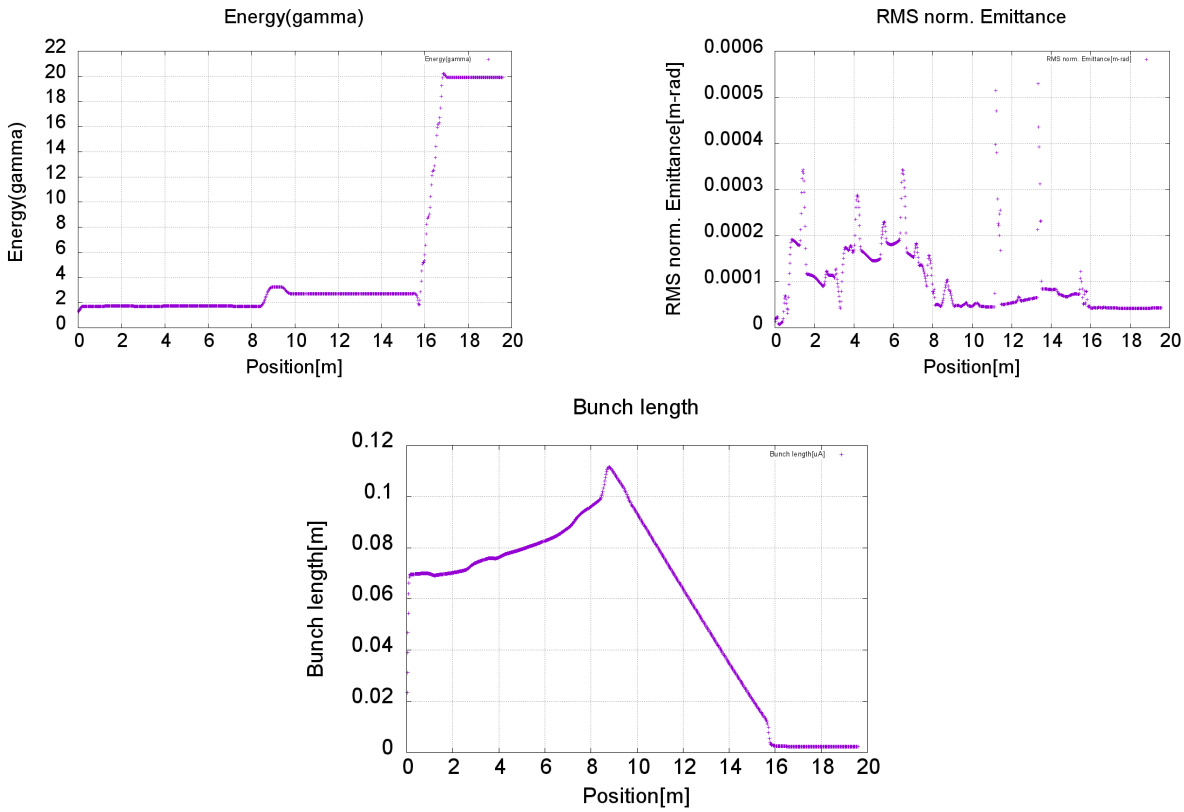

Figure I-6: Preliminary simulation results from GPT. Top left : Beam energy along the beamline; Top right: Beam emittance; Bottom: Bunch length along the beam line.

Based on the beam dynamics simulation, the injector from cathodes to end of the injector is about 20 meters long and 10 meters wide. Considering the cathode preparation system, high voltage system and build infrastructure. The building of injector dimension is about 40 meters and 15 meters.

Beam Dump

A dump beamline transports the decelerated 20 MeV beam from the main ERL to the beam dump. The beamline consists of a dipole magnet, which is a part of the spreader, and two rastering quadrupoles, which disperse the beam over the beam dump surface. The aperture of the dump beamline is large enough to transport the decelerated beam with an energy spread up to 5 MeV.

The beam dump has to be able to absorb a 1 MW heat load from the 20 MeV electron beam. The beam dump of the Cornell ERL Injector has been taken as the basis for the eRHIC dump because of the similarity of the beam parameters [7]. It is made of aluminum instead of copper to reduce neutron production. The dump consists of two sections: the body and an outer shell, containing the

cooling water. The interior shape is designed to distribute the scattered electrons as uniformly as possible around the cooled surface.

I.2.2 SRF Energy Recovery Linac

In rhe Low Risk design the electron beam will accelerated to 18 GeV after 6 passes through two SRF linacs located at 10 o'clock (IP10) and 2 o'clock (IP2) respectively, and each linac energy gain is 1.5 GeV.

Linac Configuration

The superconducting RF ERL concept allows recovery of the beam power spent for acceleration of particles by recirculating them after collisions back through the linac at an RF phase offset by 180 degrees with respect to the accelerating phase. Thus the ERL's RF systems will have to provide the power necessary to maintain stable amplitude and phase of the electromagnetic field inside the SRF cavities and to compensate for any parasitic energy losses incurred by the beam (due to synchrotron radiation, resistive wall and higher order modes). The maximum amount of SR power loss is set to 1 MW, which in turn limits the beam current at 18 GeV to 12 mA. The linac will be installed in the IP2 and IP10 straight sections (each sections is 200 meters long) of the RHIC tunnel. Parameters of the SRF linac are listed in Table I-4.

Table I-4: Linac configuration.

Energy gain [GeV]	1.5
RMS Bunch length [mm]	3
Bunch repetition frequency [MHz]	9.38
No. of RF buckets per RHIC revolution	120
Main linac RF frequency [MHz]	647.4
No. of SRF cavities	72
No of main cryomdodule	36
Linac active length [m]	84.5
Linac length [m]	198
Filling factor	0.42
Real estate gradient [MV/m]	7.58
Number of Quad and BPM	10

Figure I-7 shows the configuration of one main linac cryomodule. There are two 647 MHz 5-cell cavities in one cryomodule to provide 83.25 MeV of energy gain. There is one room temperature beam line absorber on each side of the cryomodule. The cryomodule parameters are listed in Table I-5.

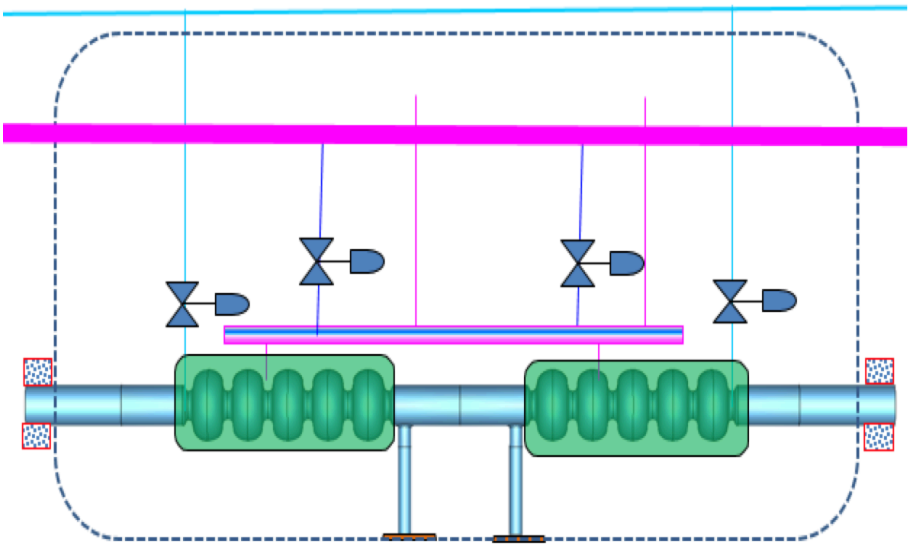

Figure I-7: One 647.4 MHz cryomodule configuration.

Table I-5: 647 MHz 5-cell cavity cryomodule.

Energy gain [MeV]	41.6
Number of cavities	2
Accelerating gradient [MV/m]	18
RF coupler per cavity	1
Operation temperature [k]	1.9
Cavity intrinsic Q factor at operating gradient	3E10
Peak resonant frequency detuning due to microphonics [Hz]	20
Qext of FPC	1.65E7
RF power per cavity [kW]	26.7
Number of RT beam line absorber	2
Max HOM power per cavity [kW]	6
Length of cryomodule with RT absorber [m]	5.5

The beam energy loss will be compensated by a separate set of cavities operating at 1.3 GHz, second harmonic of the main RF frequency. The space of 5 m in the middle of main linac is accommodated for the energy loss compensation cavities. However, the beam simulation studies are underway to explore the possibility of eliminating these cavities. Figure I-8 shows the configuration of energy compensation linac. The parameters for second harmonic cavity linac are listed in Table I-6.

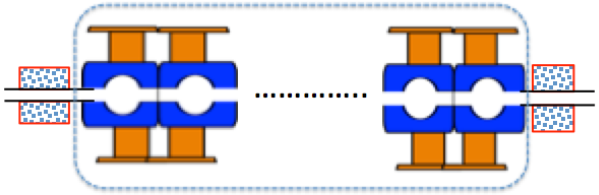

Figure I-8: Energy compensation linac configuration.

Table I-6: 2nd harmonic cavity cryomodule.

Maximum Energy loss [MW]	**1**
Frequency [MHz]	**1294.9**
Number of cell	**1**
Number of cavity	**6**
Maximum Accelerating gradient [MV/m]	**12.9**
RF coupler per cavity	**2**
RF power per coupler[kW]	**100**
Qext of FPC	**1E4~5E7**
Operation temperature [k]	**1.9**
Cavity intrinsic Q factor at operating gradient	**3E10**
Peak resonant frequency detuning due to microphonics [Hz]	**12**
Number of RT beam line absorber	**2**
Length of cryomodule with RT absorber [m]	**5**

Design of 5-cell 647 MHz cavity

The optimization of the high current SRF cavity is to maximize the HOM damping capability of the cavity while keeping the fundamental mode performance. HOM damping optimization includes two aspects: one is to reduce the HOM power by minimizing the loss factor; the other is to reduce the impedance of dipole modes to maximize the Beam-Break-Up (BBU) threshold current. The frequency of the eRHIC SRF linac cavity was decided to be 647.4 MHz (69 harmonics of RHIC bunch frequency) to accommodate the existing SRF facilities. A first design of 647 MHz cavity has been named BNL4. Figure I-9 (top) shows Superfish model of the 5-cell 647 MHz BNL4 cavity. The field profile of the fundamental mode by Superfish is shown in Figure I-9 (bottom). The fundamental mode's performance of BNL4 cavities is listed in Table I-7.

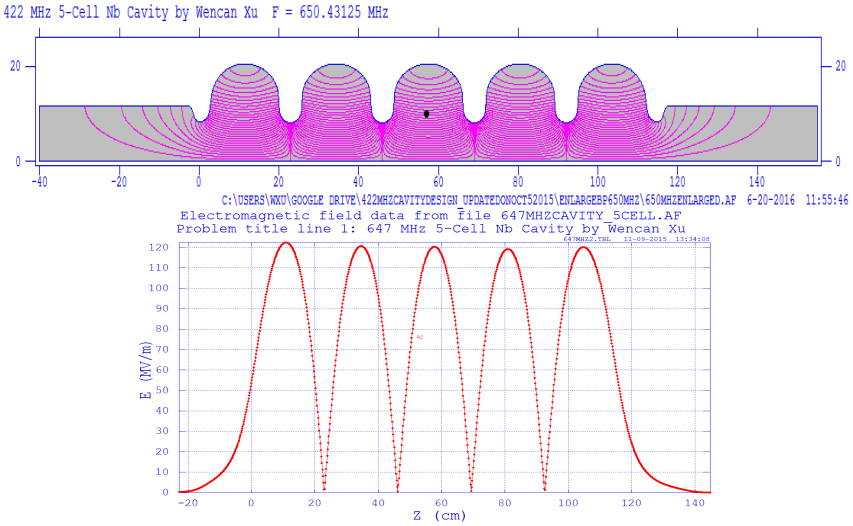

Figure I-9: BNL4 cavity configuration (top) and fundamental mode field profile (bottom).

Table I-7: RF parameters of the BNL4.

Parameters	**647 MHz 5-cell cavity**
Frequency [MHz]	647.4
Number of cells	5
Geometry factor [Ω]	273
(R/Q)/Cavity [Ω]	503
E_{peak}/E_{acc}	2.27
B_{peak}/E_{acc} [mT/(MV/m)]	4.42
Coupling factor [%]	2.8
Cavity length [m]	1.95

An average monopole mode HOM power generated by a single bunch travelling through a cavity is proportional to the bunch charge Q_b, beam current I_b, and the longitudinal loss factor k_s. The loss factor depends on the bunch length, as shown in Figure I-10. The loss factor is 2.5 V/pC for a 3mm (rms) bunch length.

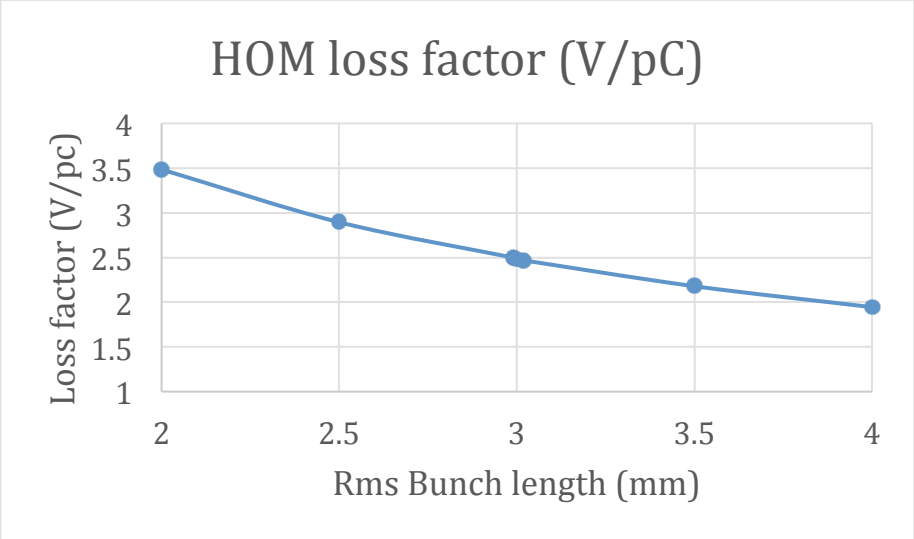

Figure I-10: Integrated loss factors of BNL4 cavity.

The BBU threshold current is inversely proportional to the transverse mode impedance ($R_d/Q^* Q_{ext}$), so minimization of the transversal impedance was another effort during the cavity design. Figure I-11 shows the impedance of the dipole modes of BNL4 cavity. BBU code simulation shows that the threshold current of BNL4 cavity for eRHIC has at least a factor of 4 above the operation beam current, for a zero frequency spread due to fabrication (usually it is around a few MHz spread) in the HOM spectrum.

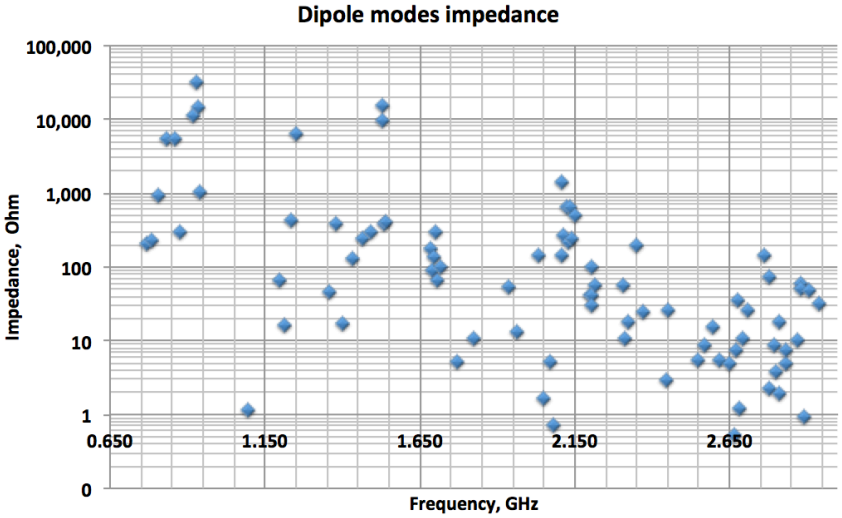

Figure I-11: Dipole modes Impedance.

Prototype of the 5-cell 647.4 MHz cavity

eRHIC is designed for a range of operating modes to allow collisions of electrons with protons ranging from energies from 40 GeV to 275 GeV. To compensate for the change in proton revolution time a frequency shift of up to 174 kHz for the 647 MHz cavity is required. ANSYS simulation shows that the cavity's tuning sensitivity is 84 kHz/mm, so the tuning range requirement for BNL4 cavity is 2 mm. With a 4 mm thickness of Nb sheet, the cavity can be tuned up to 2.0 mm without exceeding the yield strength of Nb: 7000 psi, which is shown in Figure I-12. The Lorentz detuning factor of this cavity is 0.6 Hz/$(MV/m)^2$ With middle lateral support, the frequency of the first mechanical mode is 107.2 Hz, which is a longitudinal mode.

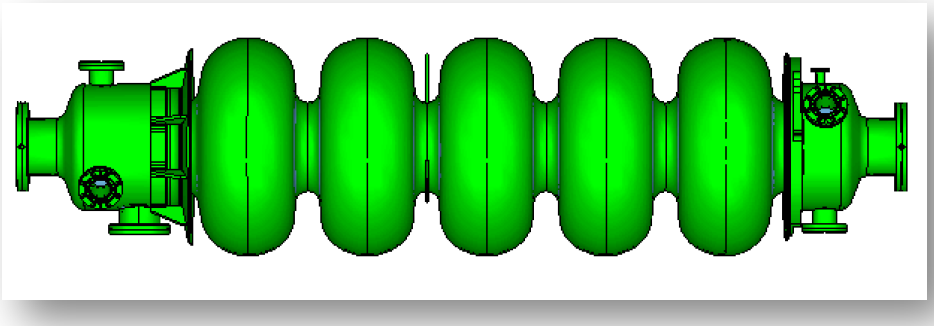

Figure I-12: The design of BNL4 cavity prototype.

The BNL4 cavity will be prototyped with frequency scaled to 650 MHz. One niobium cavity will be fabricated for cavity performance study, and one copper cavity will be fabricated for HOM damping study.

Linac Optics

The goal of the linac optics is to minimize the beta function in the linac for all passes. In the eRHIC design, it was preferred to exclude quadrupoles from the linac to minimize the total length of the linac and leave more space for the spreader-combiner sections.

When quadrupoles are excluded, the only free parameters are the initial optical functions at injection energy of the lowest energy pass. The optical functions of consecutive passes are connected by this rule:

$$\beta_n(s = L) = \beta_{n+1}(s = 0); \alpha_n(s = L) = -\alpha_{n+1}(s = 0)$$

here, *n* denote the number of times passing through the linac. This rule ensures that the optics of the decelerating stage is mirror symmetry of that in accelerating stage, when the structure of the two linacs are the same.

After optimization of the initial optical functions, the beta function of the linac through 12 accelerating passes is shown in Figure I-13, and the optics of the decelerating passes are the mirror image of the same figure.

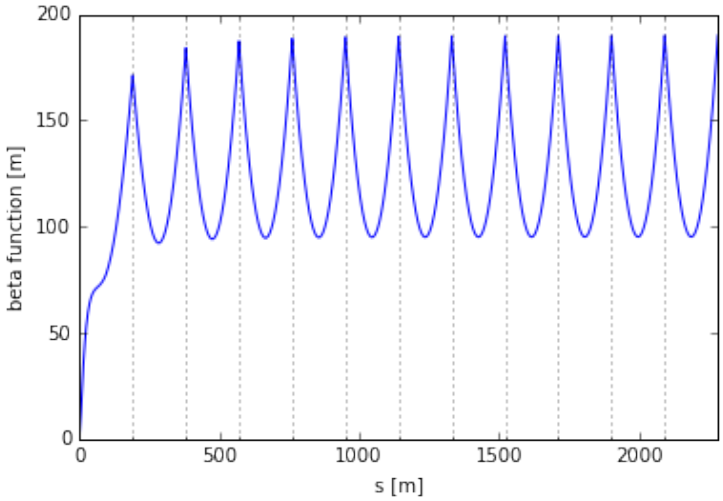

Figure I-13: The beta function in the linac for 12 passes. The horizontal and vertical optics are identical. The grid lines separate the optics of each pass.

I.2.3 Time structure

Electron-Hadron Frequency Synchronization

The eRHIC hadron beams are not ultra-relativistic, hence at the fixed closed orbit circumference the revolution frequency of hadron beam depends noticeably on its energy. In order to have the hadron and electron repetition rates synchronized in wide range of hadron energies the machine design has to incorporate a capability of varying the circumference of either hadron or electron beam transport lines. In eRHIC the hadron circumference control will be realized by radial shifts of the hadron closed orbit in hadron ring arcs. The radial orbit offsets of ±1.3 cm would provide up to 16 cm hadron circumference variation range allowing the electron-hadron synchronization in the energy range 100-250 GeV/u.

To make the synchronization at lower hadron energies the harmonic switching method is used. Switching of the ERL RF harmonic number (the ratio of the RF frequency to the revolution

frequency) down by one unit allows operating with hadron energies 43-46 GeV. And when switching to even lower RF harmonics some of lower proton energies can be accessed.

Bunch pattern

In the eRHIC *N*-pass ERL (where $N \leq 6$) ERL, there are *2N* bunches passing through each linac cross-section in one collision period (107 ns). The frequency of the RF cavity is $f_{rf} = 647.5\ MHz$, which is 69 harmonics of the collision frequency of 9.38 MHz. Therefore, there are 69 accelerating crests and 69 decelerating troughs available to accommodate *N* accelerating and *N* decelerating bunches.

The bunch pattern of the beam in the linac is determined by the path length of the recirculating passes, i.e. the time of flight from the end of one linac to the entrance of the other linac for each energy. We use $L(n)$ to represent the pass length from the entrance of linac 1 to the entrance of linac 1 on the next time, where n is from 1 to *N*. To ensure the energy recovery process, the highest (collision) energy pass should have a path length $L(N) = \left(X - \frac{1}{2}\right)\lambda_{rf}$, where *X* is an integer and λ_{rf} is the wavelength of the cavity. The multi-pass layout requires that all other lower energy pass should have pass length $L(n < N) = Y\lambda_{rf}$. The choice of *X* and *Y*, are only limited by width and length of the RHIC tunnel. Here we also need to set the length between two linacs and the phase of linac 2 to ensure that the accelerating phase in both linacs are the same. Since all the passes need to fit the existing RHIC tunnel, all path lengths should be close to the RHIC circumference 3834 m. The hadron revolution frequency satisfies $f_{h\,rev} = f_{rf}/R$, where *R=8280* is integer to guarantee the synchronization of both beams at collision point. Since all pass length of ERL are close to RHIC circumference, the ERL pass length parameters can be defined as: $x = R - X$ and $y = R - Y$.

Figure I-14 shows the desired bunch pattern for the 4-pass ERL, i.e. top energy 12 GeV, where the current is maximum in the linac. This pattern is determined by the parameters $y = 1; x = -3$. The pattern repeats every 69 RF periods, which corresponds to 9.38 MHz collision frequency.

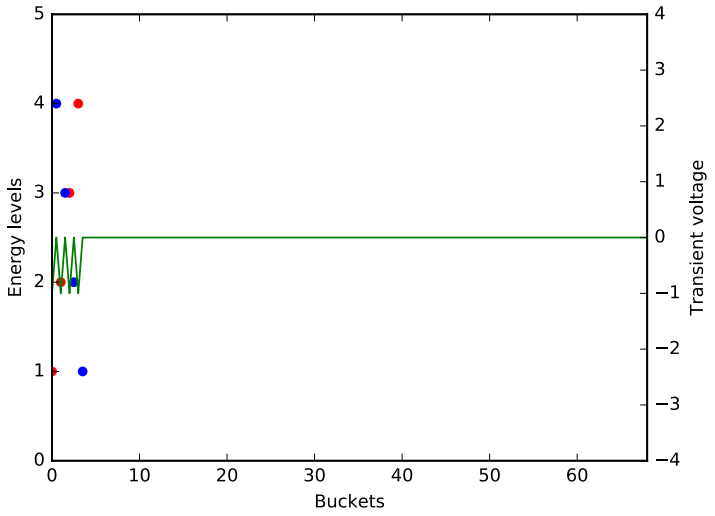

Figure I-14: The bunch pattern for 4 passes ERL. The pattern repeats every 69 RF buckets. The red dots represent the accelerating bunches and blue dots represent the decelerating bunches. The green line indicates the voltage transient effect in the cavity.

This bunch pattern is optimized with the consideration of several beam dynamics effects and technical challenges, which include

- Ionization and ion effects,
- Single bunch information detection on the beam separation,
- Cavity HOM power generation by the beam,
- Voltage transient in the cavity.

The ion effects [Sec. I.2.8] suggest that an electron bunch train gap should be implemented to counteract the ion accumulation and ion induced instability. Figure I-15 illustrates the bunch pattern with train gap of 7 collision periods.

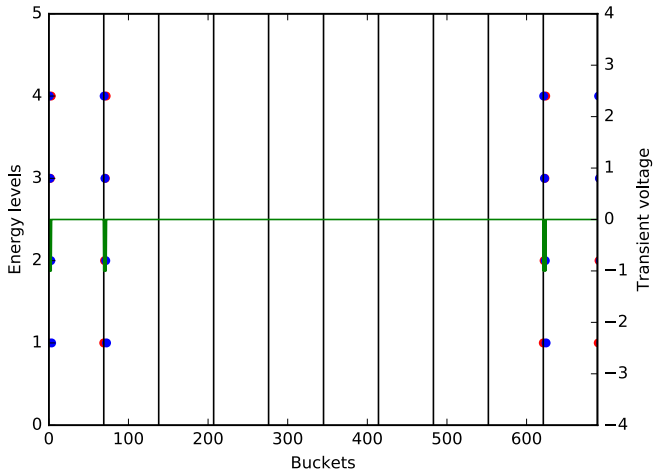

Figure I-15: The bunch pattern in presence of the electron train gap. The grid lines repeat with collision frequency 9.38 MHz**.**

The key feature of bunch pattern is minimizing the voltage transient of the beam. The stored energy in the cavity is modulated by electron beam with the same pattern. The fast fluctuation cannot be compensated by the power coupler of the cavity due to its slow response time, therefore the energy variation creates the voltage transient in the cavity (green line in Figure I-14). The unit of the transient voltage is the relative voltage variation caused by the bunch passing through the cavity, which gives:

$$\frac{dV}{V} = \frac{1}{2}\frac{dE}{E} = \frac{qV}{2\frac{V^2}{\omega(R/Q)}} = \frac{q\omega(R/Q)}{2V}$$

In the 4-pass case, the bunch charge q has highest design value. The chosen bunch pattern is designed to minimize the energy difference between the regular bunch and the diagnostic bunch.

With the pass length parameters optimized for 4 pass case, the pass length of each energy recovery passes will be determined accordingly. Therefore, when eRHIC is operated as 6-pass ERL (18 GeV top energy), the transient effect will be less than optimum. However, in such high energy mode, the bunch charge of the electron beam is also decreased by factor of 6. The transient effect is less pronounced due to the low bunch charge. Figure I-16 shows the bunch pattern for the 6-pass ERL.

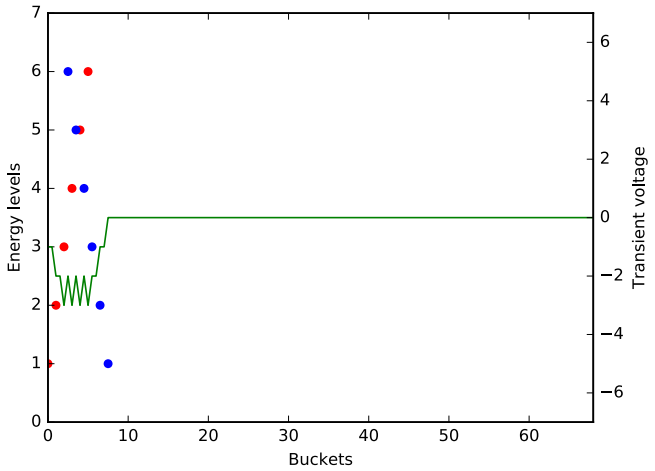

Figure I-16: The bunch pattern for 6 passes ERL. The pattern repeats every 69 RF buckets. The red dots represent the accelerating bunches and blue dots represent the decelerating bunches. The green line indicates the voltage transient effect in the cavity.

The HOM power generated by the beam also strongly depends on the bunch pattern in the linac. Different bunch patterns will generate HOM power which is different than that calculated for a single bunch. The dependence of the HOM power on bunch pattern will be explored in the course of this design studies.

I.2.4 Recirculation Pass Lattice

Introduction

A present design of the transport beam line is based on a previous work on the synchrotron lattice [8] without going through transition energy during acceleration or control of the electron time of flight. In case of the eRHIC recirculation pass lattice one wants to have isochronous one turn transport. This can be achieved by making a basic cell isochronous. The revolution time dependence on the beam momentum is given by:

$$\frac{\Delta T}{T_0} = \left(\alpha - \frac{1}{\gamma^2}\right)\frac{\Delta p}{p_0},$$

where *"α"* is the momentum compaction:

$$\alpha = \frac{1}{C_0}\sum_i D_i\theta_i$$

where θ_i is a bending angle of the dipole *'i'*. A lattice design method used here had been previously presented in [9]. To make isochronous transport the total horizontal dispersion through dipoles must have slightly negative value: $\Sigma_i D_i \theta_i, < 0$. The method is best explained by the Floquet's transformation and "normalized dispersion" function [8]:

$$\chi = \frac{D_x}{\sqrt{\beta_x}} \quad and \quad \xi = D_x'\sqrt{\beta_x} + \frac{\alpha_x D_x}{\sqrt{\beta_x}}$$

The vector $D'_x\sqrt{\beta_x}$ or $\theta_i\sqrt{\beta_x}$ presents the dipole effect on the dispersion function. These vectors need to be within the negative part of the 'χ' axis making the negative momentum compaction and providing isochronous transport as shown in the articles [8,9].

The six eRHIC beam pipe design includes two zero dispersion straight sections for matching the arcs to the straight section. The lattice design is modular: the arc basic cell provides slightly negative momentum compaction with a high filling factor and easy chromatic correction.

Basic Module of the Electron Acceleration Arc Lattice

Magnet properties in the arc module of 18 GeV arc are listed in Figure I-17. For lower energy arcs all the normalized gradients of the combined function magnet and the focusing quadrupoles Q_{F3} *are of the same value* for any energy: $K_F = -K_D = -K_{D2} = K_{F3} = 0.038\ 1/m^2$. All magnets in the arcs are combined function magnets, except the Q_{F3}. The bending dipole field in all magnets (except of the Q_{F3}) are the same value of B_{YD}= 0.241 T (at 18 GeV). The same values of the gradients and bending fields for all combined function magnets allow significant reduction in the magnet cost as their design is the same. There is only a difference in their lenghts.

Lattice functions of an arc module are shown in Figure I-17 and the lattice parameters are listed in Table I-8. Note that the dispersion function (green color) is oscillating between the positive and negative values with negative part mostly in dipoles. The arc modules use the separated function magnets.

Table I-8: Basic Parameters of the Arc Cells and Magnets.

Arc Lattice parameters	
Maximum Energy [GeV]	18
Minimum Energy [GeV]	3
Circumference [m]	3833.845
Maximum Betax [m]	23.08
Maximum Betax [m]	28.98
Max. Dispersion [m]	1.009
Horizontal Chromaticity	-35.25
Vertical Chromaticity	-33.59
Momentum Compaction α	0.0
Horizontal Sextupoles (B"l)	-0.8738
Vertical Sextupoles (B"l)	-0.9086
Horizontal Eq.Emittance E_{PX}	5.8916 nm

The betatron functions with dimensions of the elements are shown in Figure I-17. The second order sextupole tune shift with amplitude are:

$$\nu_x = 30.6493 + 0.745*10^4\ \varepsilon_x + 0.204*10^4\ \varepsilon_y$$
$$\nu_y = 27.6723 + 0.204*10^4\ \varepsilon_x - 0.597*10^4\ \varepsilon_y$$

The combined function magnets reduce significantly the synchrotron radiation as the bending radius becomes larger. The energy loss of 18 GeV electron on one turn is 33 MeV.

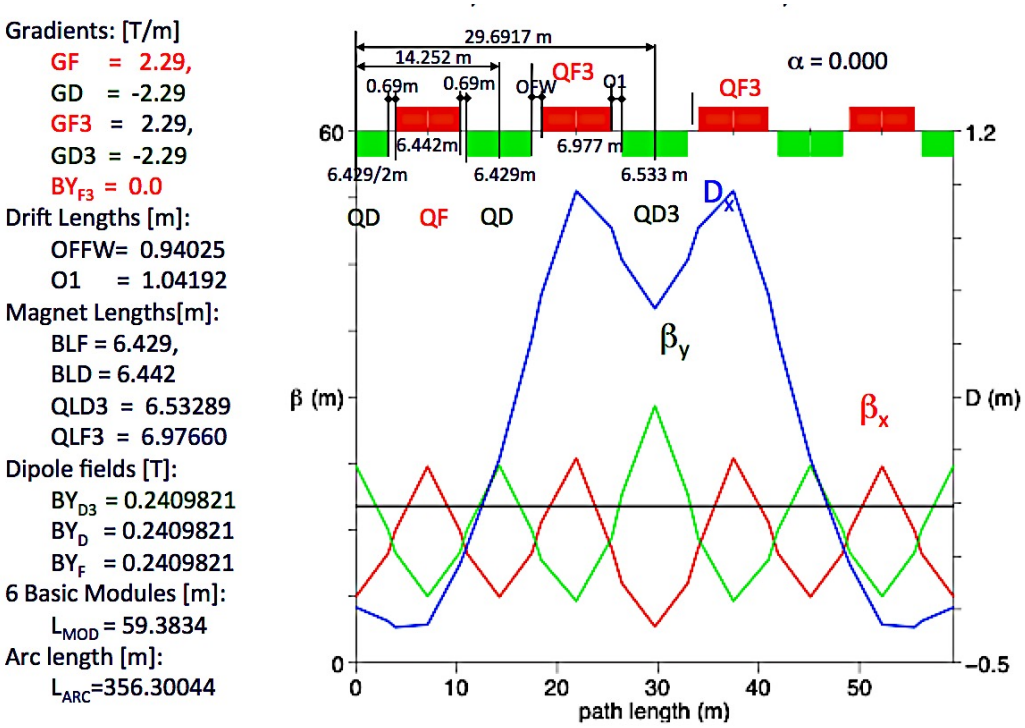

Figure I-17: Betatron functions in the basic arc cells (six of these cells make one arc).

The lattice functions at other 5 lines are identical to the ones shown in Figure I-17.

I.2.5 Magnet Design for the Cell

In this section we discuss the type of magnets which can be used in the cells which comprise the six recirculation arcs. There are three types of magnets under consideration that can be used in the cell of the arcs; a) Iron dominated electromagnets, b) Iron dominated permanent magnets, and c) Halbach type of permanent magnets. Presently the electromagnet is being considered as the baseline choice, while permanent magnet designs as possible, cost efficient, alternatives. The beam optics of the arc-cell is shown in Figure I-17 calls for a magnet which can provide a dipole strength of ~0.2 [T] and a quadrupole strength of ~2 [T/m]. A magnet with these properties is a combined function magnets or a superposition of a dipole and a quadrupole magnet as we will describe in the following subsections.

Iron dominated electromagnet

Figure I-18 is a cross section of one of the three possible magnet designs that can be used in the cell of the recirculating arcs. The blue area is the soft magnetic iron, and the red areas are the current currying conductors. The green traces shown in the figure are the equipotential vector lines.

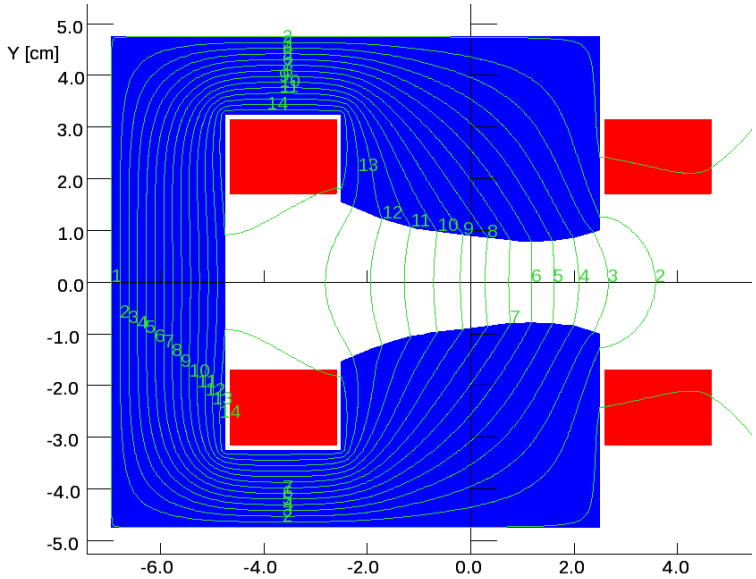

Figure I-18: The cross section of an iron dominated electromagnet. The green lines are the vector equipotential lines.

This magnet provides 0.2 T dipole field and a quadrupole field strength of 0.0248 T at a radius of 0.9 cm. This quadrupole field strength is equivalent to 2.75 T/m. The pole face of the magnet is designed to generates a zero strength of sextupole and octupole multipoles. The current density in the current currying conductors is ~500 A/cm^2. This c-type magnet provides open space for the synchrotron radiation to escape without interaction with any part of the magnet.

Iron dominated permanent magnet

The iron-dominated permanent magnet whose cross section is shown in Figure I-19 generates an equivalent magnetic field as the iron dominated electromagnet discussed in the previous subsection. The soft magnetic iron is depicted by the dark blue color and the permanent magnet material of NdFeB-N35 is the area with the ciel color. Like the electromagnet the magnetic field multipoles of this magnet are: B_{dip}=0.2139 T, B_{quad}=2.8 T/m, B_{sext}~0.0 T/m^2, and B_{oct}~0.0 T/m^3. Unlike the electromagnet, the iron dominated magnet does not need a power supply to operate, however it generates higher fringe field at the region beyond the return iron x<-6.0 cm. This fringe field can be reduced to acceptable levels by modifying the magnet.

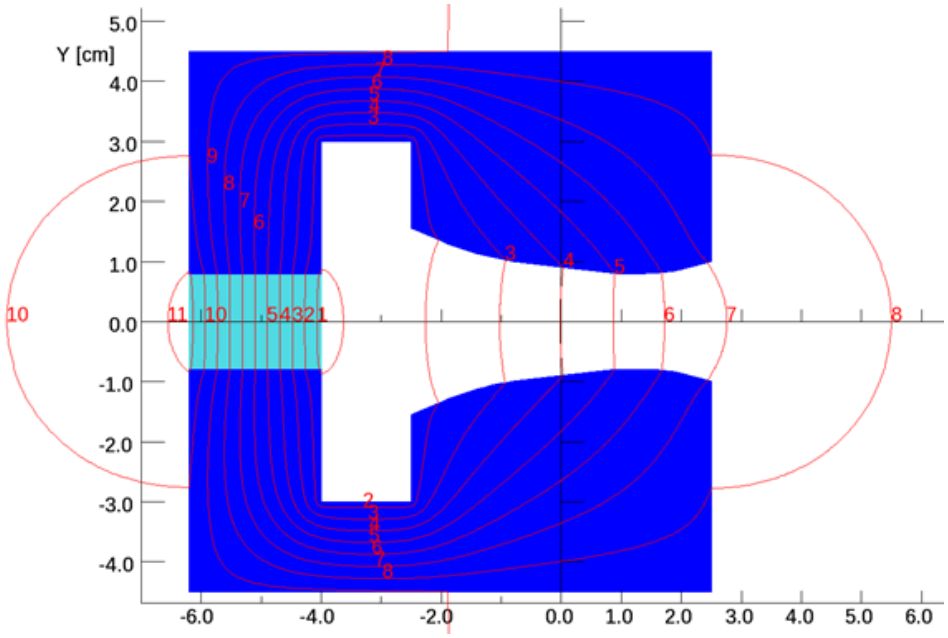

Figure I-19: The cross section of an iron dominated permanent magnet. The red lines are the vector equipotential lines.

Halbach permanent magnet

The required dipole and quadrupole strength of the cell magnets can also be provided by the superposition of two Halbach type permanent magnets, as shown in Figure I-20 (left). This magnet is

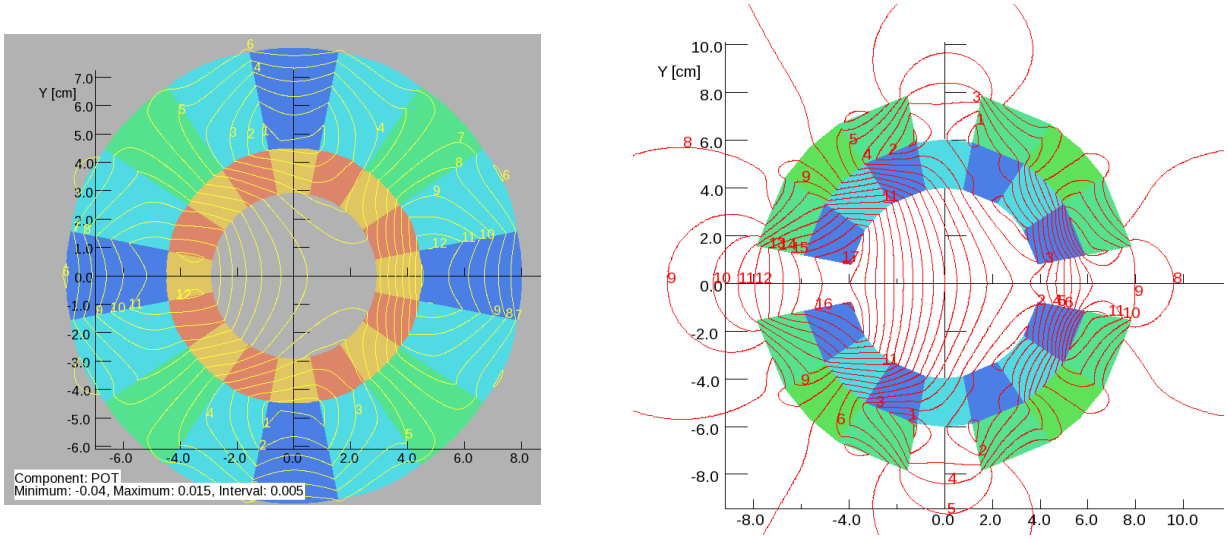

Figure I-20: (Left) The cross section of the superposition of a dipole Halbach magnet (inner wedges) and a Halbach quadrupole magnet (otter wedges). (Right) A modified version of the Halbach magnet appearing in the left picture. Some of the wedges have been removed to allow the synchrotron radiation to escape without damaging the permanent magnet material, and also to keep the correct symmetry of the quadrupole magnet. The yellow and red lines are the vector equipotential lines.

comprised of two rings made of permanent magnet wedges. The inner ring provides the dipole magnetic field and the outer ring that of the quadrupole. A modified version of this magnet is shown

on the right picture where some of the permanent magnet wedges have been removed to allow the synchrotron radiation to escape without damaging the permanent magnet material, and also to keep the correct symmetry of the dipole and quadrupole magnets. The yellow and red lines are the vector equipotential lines. The high saturation of the permanent magnet material (μ~1.0) allows the linear superposition of the dipole and quadrupole fields generated by the two Halbach magnet rings. This particular design of the magnet on left picture generates a dipole field of 0.4 T and a quadrupole field of 7 T/m. The fringe field emanating by the magnet on the right can be easily suppressed by placing a magnetic shield around the magnet without affecting the main field of the magnet. By adjusting the easy axes of the permanent magnet wedges we have minimized the allowed multipoles which are not desired. Many measurements have already been performed on the magnetic field of the Halbach type quadrupole magnets using the rotating coil technique. One of the setups for the measurement is shown in Figure I-21.

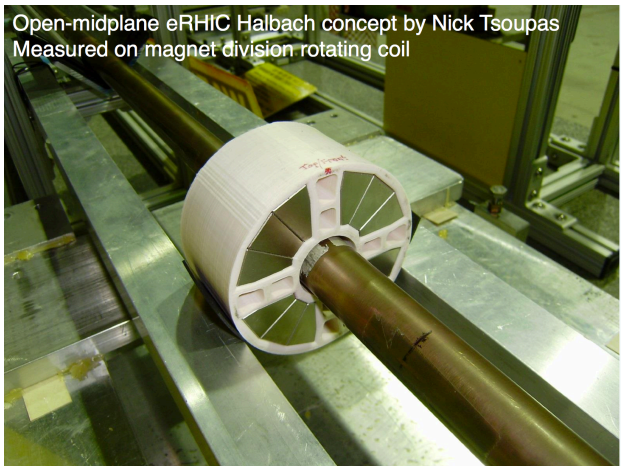

Figure I-21: Magnetic measurements of the Halbach type magnet considered for eRHIC.

I.2.6 Splitter and Combiner

Introduction

The splitter/merger sections of the eRHIC are a set of 6 beam lines which is designed to transports the beam bunches from the exit of the 1.5 GeV ERL to the entrance of the recirculating arcs (splitter in Figure I-22) and from the recirculating arcs to the entrance of the ERL (merger in Figure I-22). Each beam line transports the electron bunches with specific energy.

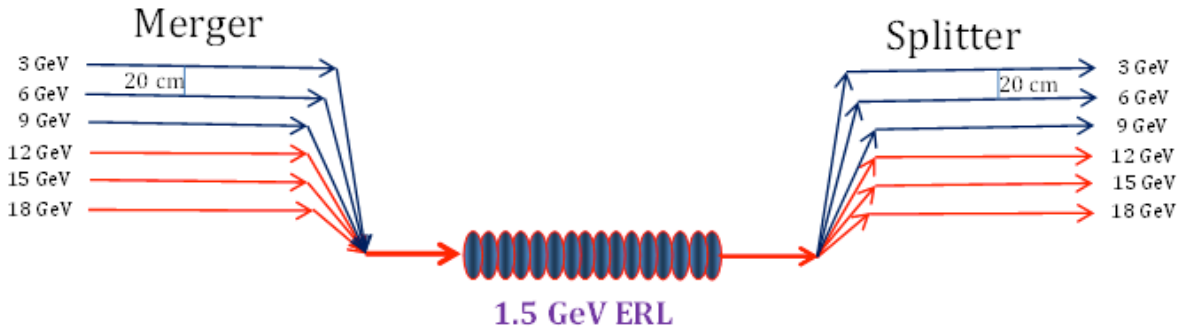

Figure I-22: Schematic diagram of the splitter/merger section of the electron accelerator. The merger is a set of 6 beam lines that merges the electron bunches from the recirculation arcs to the ERL. The splitter is a set of 6 beam lines that separates the electron bunches exiting the ERL and distributes them to the recirculation arcs.

There will be two splitter/merger sections in the electron accelerator of eRHIC, one at the 2 o'clock straight section of RHIC where one of the 1.5 GeV ERL will be placed, and the other at 10 o'clock straight section of the other 1.5 GeV ERL. The layout of the eRHIC six arm splitter is shown in Figure I-23.

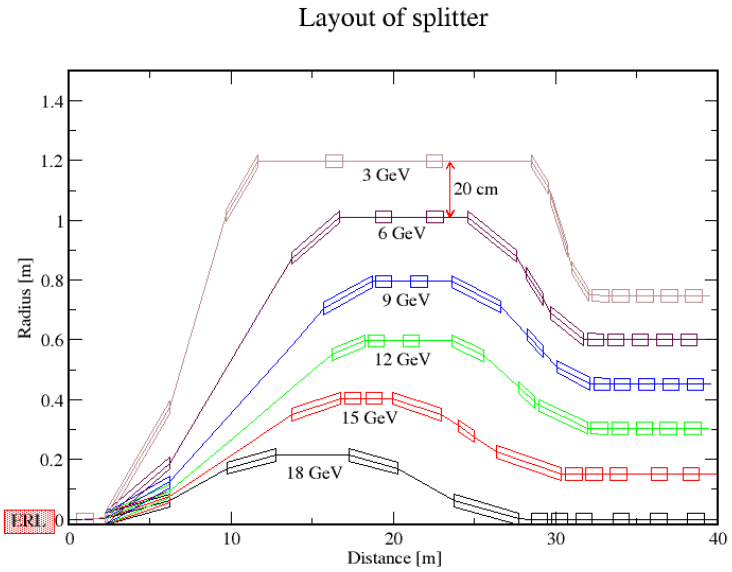

Figure I-23: The layout of the six-beam-line splitter of the eRHIC.

The eRHIC splitter is an approximate replica of the CEBAF splitter/merger. Figure I-24 is a drawing of the layout of the magnets of the 6 lines of the CEBAF splitter.

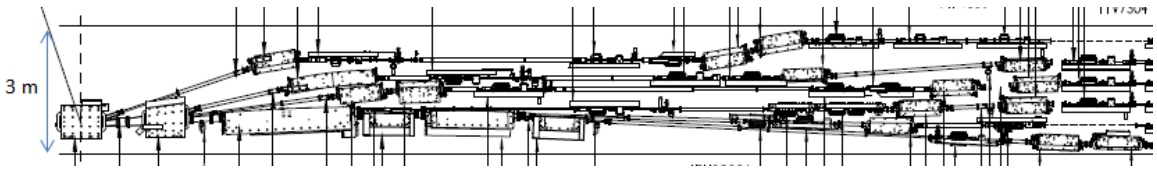

Figure I-24: A drawing with the layout of the magnets of the four beam line CEBAF's splitter**.**

The functions of the Splitter/Merger

Below we list the most important functions of the splitter/merger:

- Transport and optically match the electron bunches from the exit/entrance of the ERL to the entrance/exit of the recirculating arcs.
- Act as a beam-diagnostics and beam-control-lines of the electron bunches.
- Adjust the betatron phase advance to minimize the Beam Break Up (BBU) effect.

The isochronicity of the electron bunches in the recirculating arcs will be controlled by adjusting the length of each arc. The arcs will also adjust the R_{56} matrix element which controls the isochronicity of the electrons with different momentum within the bunch.

Path length difference of the splitter/merger lines.

The splitter/merger beam lines introduce different path lengths for the bunches having different energies. Table I-9 lists the path length introduced by the various beam lines of the splitter/merger. The arc which is connected with a particular beam line of the splitter/merger will compensate for the path length increase introduced by the beam line to make the recirculation of the bunches isochronous.

Table I-9: The values of the path-lengths introduced by the beam lines of the splitter/merger.

KE [GeV]	Splitter/Merger Path-length [cm]
18.00	0.54
15.00	1.05
12.00	1.88
9.00	3.05
6.00	5.59
3.00	12.74

The beam optics

Each beam line of the splitter/merger matches the beam parameters (α_x,β_x, α_y,β_y) and the dispersion functions (η_x, η'_x, η_y, η'_y) of the ERL with those of the various arcs. Figure I-25 is an example of such an optical matching of one of the beam lines.

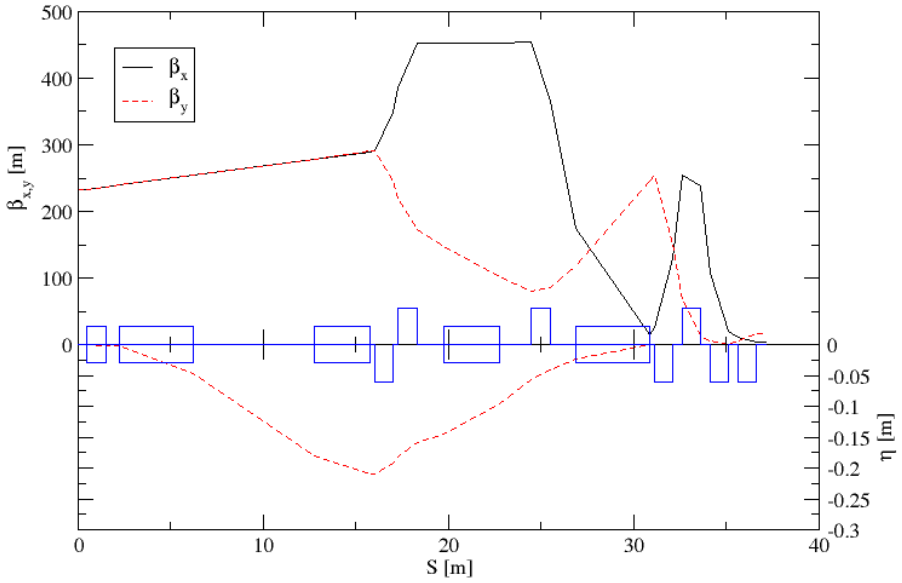

Figure I-25: Plot of the (β_x, β_y) and (η_x, η_y) functions vs distance for of the beam lines of the splitter.

Magnet size consideration of splitter/merger

The splitter /merger must fit in the RHIC tunnel which has an available transverse cross section of ~3 m to accommodate the 6 beam lines. In this design of the splitter/merger we have separated the beam lines by 20 cm and we design the magnets to fit within this available space. Figure I-26is a schematic diagram of three consecutive beam lines with two magnetic elements in each of the two beam lines. The maximum magnetic field of the dipoles in the splitter/merger is 0.45 T.

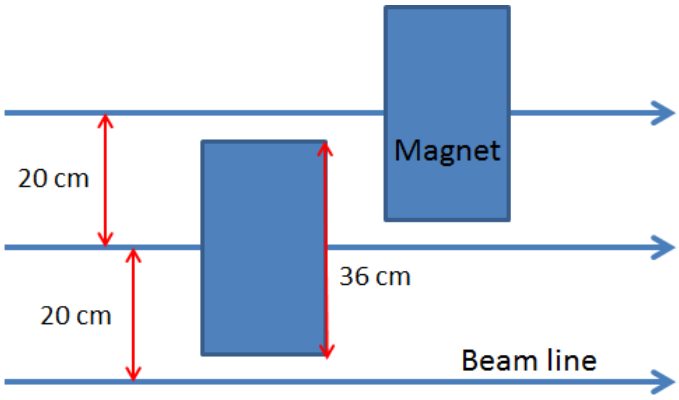

Figure I-26: Schematic diagram of three consecutive lines of splitter/merger with two magnetic elements in two of the lines. The separation of the beam lines center to center is 20 cm therefore we keep the transverse size of the magnetic elements below 36 cm**.**

An alternative way of minimizing the transverse size of the magnets is to use hybrid type of magnet made of permanent magnets and electromagnets. Figure I-27 is a schematic diagram of a hybrid dipole (blue and red rectangles on top) and a hybrid quadrupole (blue and red rectangles below), with the permanent magnets flunked by two low strength electromagnets of the same multipolarity. The cross section of a quadrupole and dipole permanent magnets is shown on the left and right side at the bottom of Figure I-27. The cross section of such magnets is less than 15 cm including the

magnetic shielding shown by the two blue rings surrounding the quadrupole magnet on the bottom left. Similar magnetic shielding should exist around the dipole magnet. The red rectangles which flunk the permanent magnets are low strength electromagnets of the same multipole for fine field control.

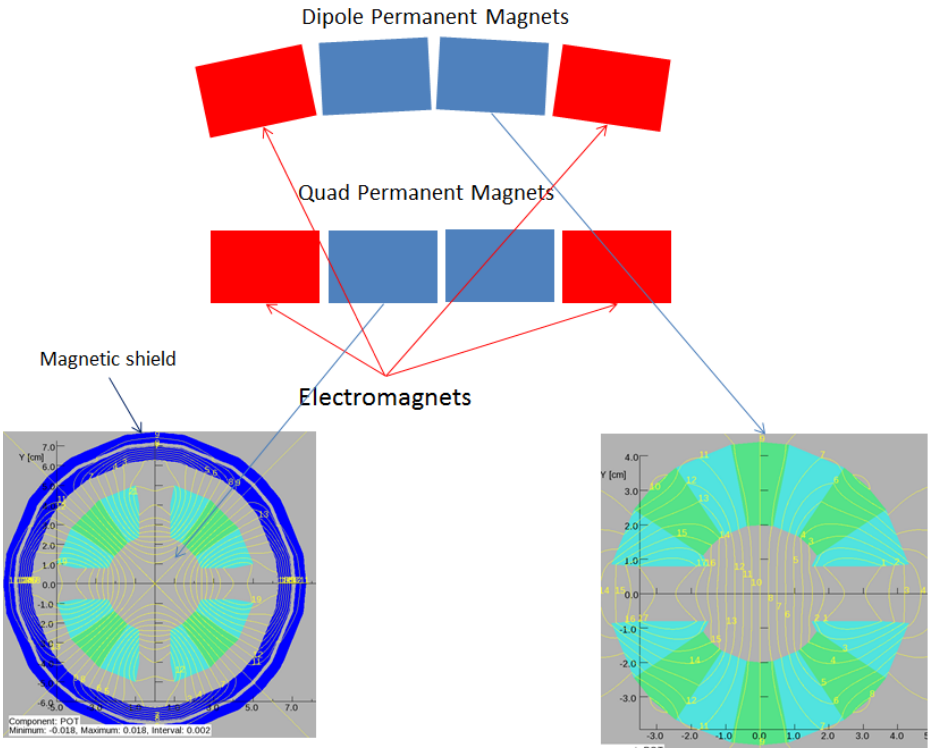

Figure I-27: Schematic diagram of a hybrid dipole (blue and red rectangles on top) and a hybrid quadrupole (blue and red rectangles below), with each element flunked by two low strength electromagnets of the same multipolarity. The cross section of a quadrupole and dipole permanent magnets is shown on the left and right side at the bottom of the figure. The cross section of such magnets is less than 15 cm including the magnetic shielding, shown as the two blue rings surrounding the quadrupole magnet. Similar magnetic shielding should exist around the dipole magnet shown on the left. The red rectangles which flunk the permanent magnets (blue rectangles) are low strength electromagnets of the same multipolarity as the permanent magnets, for fine field control.

I.2.7 Start-to-end Simulations

The current start to end simulation of the multi-pass ERL of eRHIC starts with the injection energy 20 MeV at the entrance of the linac. The beam is recirculated through the linacs via six recirculation loops along RHIC ring until it reaches collision energy (18 GeV) and then decelerated down to 20 MeV and steered to the dump line. The simulation includes the 2 linacs through which the beam passes 6 times, as well as the 12 recirculating beamlines that transport the beam of various energies during acceleration and deceleration stage. The design of the spreader and combiner is on-going. They are represented by the 6-D linear transfer matrix to match the optics function and time of flight. Figure I-28 illustrates the components and sequence of the start-to-end simulation.

Figure I-28: The components and sequence of start-to-end simulation.

Two codes are now being used for this purpose, Elegant [10, 11] and Zgoubi [12, 13]. In Elegant, we use uses 4th order symplectic integrator to track the particles through the linac and the beamlines with wake field effects. Zgoubi is a stepwise ray-tracing code. Zgoubi also provides the unique feature of spin tracking. In this design, we start the simulation using Elegant and the simulation using Zgoubi will follow.

In Elegant simulation, both the 650 MHz fundamental cavities and the second harmonic cavity are included in the linac. All cavities have their phases according to the arriving time of the simulated bunch. The voltage of the second harmonic cavity is determined by compensating the accumulated energy loss due to synchrotron radiation. Currently the synchrotron radiation of spreader and combiner are not included, since they are now represented by matrices. However, the contribution is expected to be less than 15%. When they are included, the voltage of second harmonic cavity will be adjust to compensate the loss.

Figure I-29 shows the longitudinal dynamics of the start-to-end process for a 3mm rms bunch length beam. The energy and rms energy spread of the electron beam in the entire process is shown in the left, while the final longitudinal phase space distribution is shown in right. The energy spread of the electron is contributed from the RF curvature and the synchrotron radiation. The energy spread due to the RF curvature when the beam is accelerated on-crest, can be compensated in the decelerating stage if the decelerating phase is π apart. The residue energy spread is dominated by the longitudinal emittance growth due to nonlinear longitudinal transport and synchrotron radiation effect which cannot be compensated.

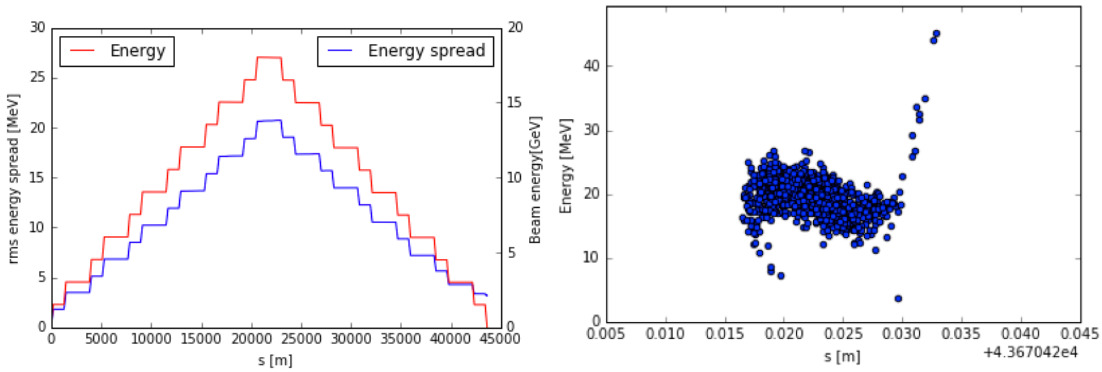

Figure I-29: Left, the beam energy(red) and rms energy spread(blue) of the electron beam through the start-to-end transport. Right, the longitudinal phase space due at the dump energy.

The further longitudinal dynamics is in progress, aiming on determine the following topics:

- Investigate the possibility of longer bunch length.
- Possibilities of using off-crest accelerating and deceleration to compensate the energy loss.

- Tolerance of pass length and the compaction factor of the energy recovery passes.

The transverse dynamics study is also in progress, which will ensure the beam emittance preservation of the electron beam in the energy recovery process, the tolerance of the magnet misalignment error and gradient error, halo effect and the orbit/optics correction algorithm.

I.2.8 Beam Dynamics Effects

Various collective effects were studied and three effects have been recognized as most important: the energy losses and energy spread due to collective effects, multi-pass beam breakup instability due to high order modes of SRF cavities, and the fast beam-ion instability.

Energy losses and energy spread

The following effects are investigated for potential energy losses and resulting energy spread: coherent synchrotron radiation (CSR), longitudinal resistive wall impedance, the higher order modes (HOM) of the SRF cavities, wall roughness of the beam pipe and synchrotron radiation. Table I-10 summarizes our estimations for the current design. As shown in the table, we expect that the energy loss due to CSR will be suppressed by the shielding effects of the vacuum chamber of FFAG beamlines. Furthermore, the wall roughness of the extruded aluminum vacuum chamber can be reduced to sub-micron level[†] and its contribution to the energy spread is estimated to be negligible compared with other effects. The total power loss is about 2.5 MW, which has be compensated by a dedicated system of second harmonic RF cavities or by off-crest deceleration of the electron beam in main linac cavities. The full energy spread of the electron beam at its last pass through the linac is comparable or larger than its final energy going to the beam dump. The possible techniques to reduce this energy spread are under exploration.

Table I-10: energy losses and energy spreads due to various collective effects with the top electron energy of 12 GeV (top) and 18 GeV (bottom).

	CSR	Machine impedances	Wall roughness	Synchrotron Radiation	Total
Energy loss, MeV	Suppressed	1.4	Negligible	12	13.5
		2.16		89	91
Full energy spread, MeV	Suppressed	2.2	Negligible	0.4	~2.2
		3.4		2	~4

Multi-pass beam breakup

Multi-pass beam breakup (BBU) is the major limiting factor of the average current in ERL [14]. When there is positive feedback between the HOM excitation and the momentum change due to the HOM, the system become unstable. In multi-pass ERL with long linac, the BBU threshold current cannot be determined by theoretical prediction. Instead, the BBU threshold for eRHIC is calculated by using the BBU simulation code GBBU [15]. The higher order mode frequencies and the

[†] We measured 0.2 μm rms surface height variation from a sample aluminum beam pipe provided by ANL.

corresponding R/Q can be found in Figure I-11. Besides the cavity HOMs, the phase advance between linac and the time structure of the electron beam in linac also play an important role in determining the BBU threshold of the beam current.

The calculation is in progress. In earlier studies of eRHIC ERL with 12 pass with same 650MHz cavity, the threshold is determined to be 53mA when there is no HOM frequency spread. The threshold current increases to over 100mA when 1e-3 rms frequency spread of each HOMs is assumed.

Fast beam-ion instability

The fast beam-ion instability is caused by electron beams resonantly interacting with ions generated from ionizing the residual gas molecules. The instability is most pronounced when the ions are trapped in the beam passage by the periodic focusing force provided by the beam. In our current analysis, the ion is assumed to be CO^+ with 1 nTorr pressure.

A weak-strong code has been developed to simulate the fast beam-ion instability in the recirculating passes, which takes into account the non-linear space charge forces of the electron bunches and simultaneously simulates electron bunches from all energy passes. The simulation done for beam parameters of previously studied FFAG eRHIC design agreed well with the theoretical estimation in the linear space charge limits and, in the absence of a gap between bunch trains, showed significantly slower but persistent growth with the non-linear space charge force being adopted. However, no growth of the coherent electron oscillation is observed from the simulation with a 950 ns gap introduced between two adjacent bunch trains, as shown in Figure I-30 . The similar studies will be done for the Low Risk design parameters.

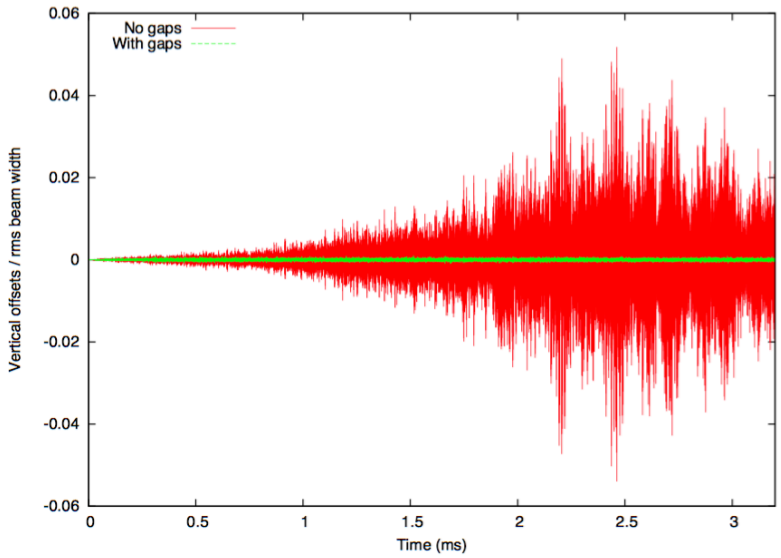

Figure I-30: Simulation results of FBII in the low energy FFAG ring for the nominal design of FFAG eRHIC. The abscissa is time in unit of millisecond and the ordinate is the offset of electron bunches, as observed at the exit of the ring. The red data points show the bunch offsets in case that there is no gaps between bunch trains and the green data points show the bunch offsets when clearing gaps of ~950 ns are introduced. The simulation assumes 8 mA of average electron beam current and 23 passes of the FFAG arcs with a top energy of 20 GeV.

I.2.9 Beam Halo

Understanding all potential sources contributing to the electron beam halo and associated beam loss is crucial for the successful operation of eRHIC based on the recirculating linac approach. The evaluated beam halo size dictates a proper choice of magnet apertures of re-circulating loops. The application of a collimation system (especially, to address the halo produced by the injector) may also be needed.

To our present best knowledge major sources of the halo are: the injector halo (scattered laser light, space charge, …); beam-beam effects; beam-gas scattering; Touschek scattering; linac cavity dark current; beam transport errors. Simulation tools and techniques are available to evaluate or estimate each of the halo sources, and they have been used for the halo evaluation for various past modifications of the eRHIC design. Typical values seen for beam losses for 6 MeV energy acceptance are several tens pA for beam-gas scattering and several hundred pA for Touschek scattering. And Figure I-31 plots the beam power loss at a given aperture at different electron energies during deceleration process. The beam power loss was calculated using the full beam distribution after electrons passed the collision point. Thus, it includes the halo created by the beam-beam interactions (see section I.2.10). The recirculating loop magnet must have enough aperture to transport this halo during deceleration.

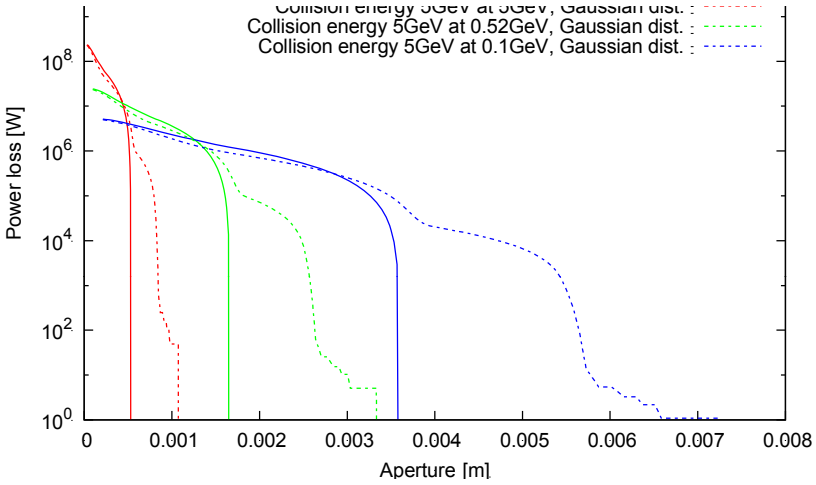

Figure I-31: Beam power loss at a given aperture and various energies resulting from the beam halo produced by the beam-beam effects. The results are shown for two types of transverse distribution before the collision point: the Gaussian distribution (3σ cut) and Beer-Can distribution. .

I.2.10 Beam-Beam Effects

Beam-beam effects present one of the major restrictions in achieving higher luminosities. eRHIC adopts the linac-ring scheme to remove the beam-beam effect limit of the electron beam and aims for higher luminosity than a traditional ring-ring scheme. There are several challenging effects in the linac-ring scheme, including the electron disruption effect, the pinch effect, the ion-beam kink instability and the ion beam heating due to electron beam noise. Since no linac-ring collider existed the linac-ring beam-beam interaction must be thoroughly studied with simulation codes.

Electron disruption effect rises due to the large beam-beam parameter of the electron beam proposed in eRHIC. The strong nonlinear beam interaction field will distort the electron beam distribution and the large linear tune shift leads to significant mismatch between the designed optics and the electron beam distribution. The effect was studied in detail in [16]. Figure I-32 shows the beam distribution after the collision and the electron beam size and emittance evolution in the opposing ion beam. The emittance growth and beam size blow-up due to the electron beam disruption effect are in acceptable range and will not affect the beam transport and energy recovery process in the beam decelerating stage.

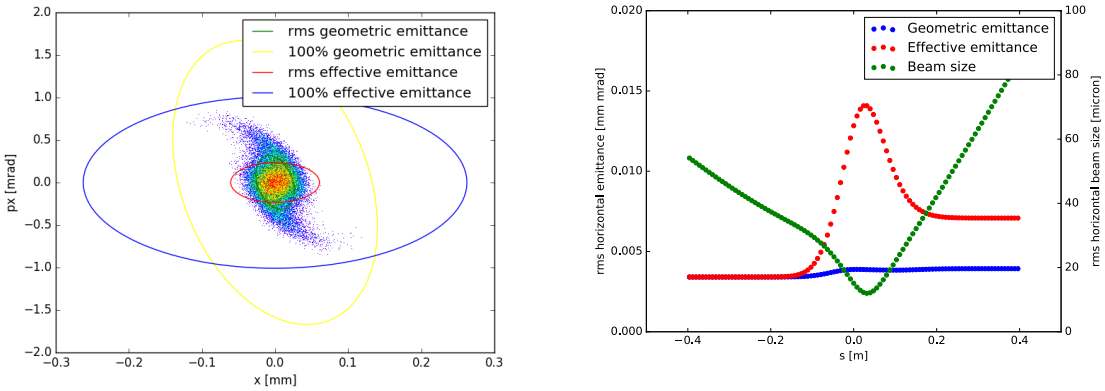

Figure I-32: Left, electron beam distribution after the collision in transverse phase space (x-p_x); right, the electron beam parameter evolution in the opposing ion beam, e-beam travels from right to left.

The pinch effect describes the electron beam size shrinking in the interaction region due to the focusing beam-beam force, as shown in Figure I-32. This effect will naturally boost the luminosity. For the design parameters, the pinch effect will boost the luminosity from $0.9 \cdot 10^{33}$ cm-2s-1 to $1.27 \cdot 10^{33}$ cm-2s-1. However, this effect also enhances the local beam-beam force to the opposing ion beam, which needs careful dynamics aperture study (Figure I-47).

For the ion beam, the largest challenge is the kink instability. The instability arises due to the effective wake field of the beam-beam interaction with the electron beam. The electron beam is affected by the head of the ion beam and passes the imperfection of the head portion to its tail. References [17] and [18] describe the instability in detail. The work in [18] predicts the threshold of the instability with two theoretical models (two-particle model and multi-particle circulant matrix model), as shown in Figure I-33. The eRHIC parameter exceeds the threshold, therefore a fast (few thousand turns) deterioration of the ion beam is expected if no countermeasure is implemented. Simulations also indicated that the current chromaticity in RHIC cannot suppress the instability.

In reference [18], an innovative feedback system is presented as an effective countermeasure. In this feedback system, one electron bunch will be slightly steered transversely based on the feedback information of the previous electron bunches after collision. These electron bunches interact with the same ion bunch. The feedback system can successfully suppress the kink instability in a cost effective way, since there is no RHIC modification required.

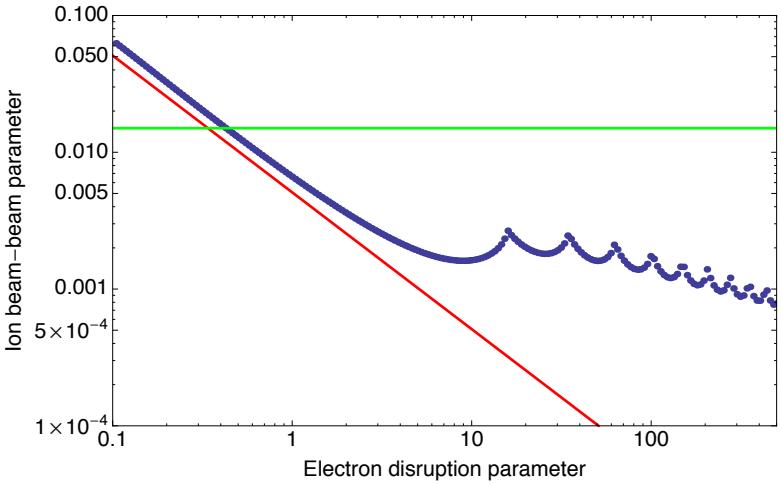

Figure I-33: The threshold of kink instability, with choice of the synchrotron tune 0.004. The Blue dots denote the threshold calculated from macro-particles circulant matrix method. The red line represents the simple threshold form from simple two-particle model. The green line corresponds to the constant beam-beam parameter of 0.015, which is design beam-beam parameter of ion bunch in eRHIC.

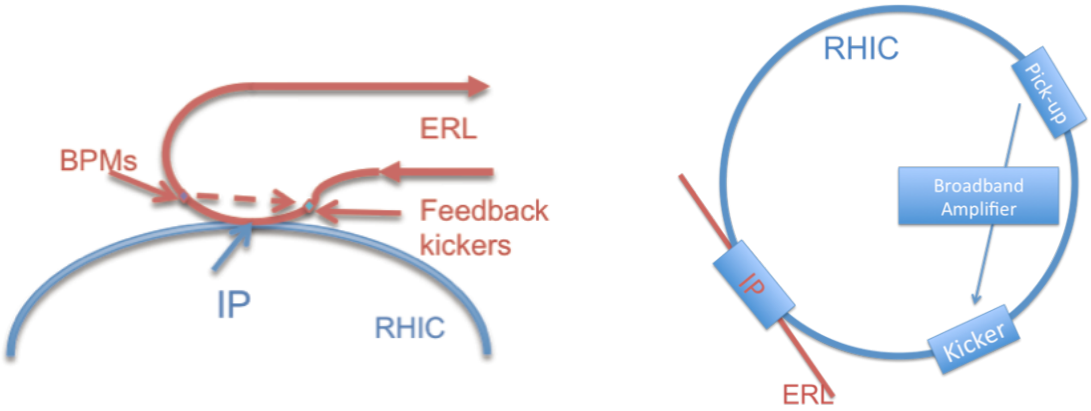

Figure I-34: Left, dedicate feedback system of the electron accelerator to mitigate the kink instability; right, the pickup-kicker feedback system in RHIC for mitigating the kink instability.

An alternative traditional feedback system for the kink instability is also studied in [19]. It consists of a pickup, a kicker and the broadband amplifier between them. For the eRHIC parameters, the minimum bandwidth is determined up to 200 MHz from the simulation result.

The noise carried by the fresh electron beam may heat up the ion beam due to the beam-beam interaction. The random electron beam offset at the IP causes dipole-like errors for the ion beam, while the beam-size and intensity variation at the IP lead to quadrupole-like errors. In this design, due to the absence of cooling, there is no practical mechanism to compensate the quadrupole kick effect. The quadrupole noise will cause the exponential growth of the ion beam size,

$$\sqrt{\langle x^2\rangle(t)} = \sqrt{\langle x^2\rangle(0)}e^{t/\tau}\,;\tau = \frac{T}{4\pi^2\xi_i^2}\frac{f^2}{\langle\delta f\rangle^2}$$

Taking advantage of the low beam-beam tune shift of the ion beam, the rising time the ion beam size due to white noise is 5.6 hours if the relative quadrupole error is 0.001.

I.2.11 Beam Polarization

The polarized electron beam is produced from the polarized source, with a polarization of ~85-90%, and the task is to preserve this high polarization through the acceleration cycle up to the collision points. During the beam acceleration electron spin is oriented vertically in the recirculating passes. Since eRHIC experiments call for longitudinal polarization a spin rotator is inserted into the highest energy beam line. The spin rotator converts the vertical polarization of the electron beam in the arcs to a longitudinal polarization at the experimental detector. The state-of-the-art electron spin rotator that was used in the electron-proton collider HERA (DESY, Germany) [20] was 56 m long. It employed a sequence of interleaved vertical and horizontal dipole magnets to transform the vertical spin of 27 GeV electrons to the required orientation in the horizontal plane. The vertical orbit excursion inside the spin rotator was quite large – about 20 cm – thus requiring some of the rotator magnets to be shifted vertically from the plane of the HERA electron ring.

Table I-11: Spin rotator parameters.

Parameter	sol1	sol2
Field integral range [Tm]	2 – 40	0 – 127
Solenoid length (at 7 T max field)	5.7	18.1
Bending angle from the IP [mrad]	92	46
Location in the RHIC tunnel	D9 – D10	D6 – Q8

The eRHIC spin rotators must operate over a large energy range, from 5 GeV to 20 GeV. Since the orbit excursion in the dipole magnets scales inversely with the beam energy, a HERA-type rotator leads to one meter orbit excursions of 5 GeV electrons. Further, the synchrotron radiation power (per meter) produced by 20 GeV eRHIC electrons is considerably larger than the 27 GeV electrons in HERA, due to the much large electron current. Reducing the linear power load requires further increasing the rotator length and, correspondingly, the vertical orbit excursion. Therefore, the only practical solution is a spin rotator based on strong solenoid magnets. Solenoidal Siberian Snakes have been used in electron accelerators operating in the 0.5 GeV to 1 GeV range [21]. The integrated longitudinal field necessary to rotate the electron spin by 90 degrees, from the vertical to the horizontal, is

$$BL\ [Tm] = 5.240\ E\ [GeV]$$

A solenoid-based scheme for eRHIC using two rotators is shown in Figure I-35. The combination of rotators (sol1 and sol2) and bending arcs allows to realize the exact longitudinal orientation of electron spins in the energy range from 5 GeV to 20 GeV. Optimization of solenoidal spin integrals led to the parameters listed in Table I-11. Figure I-36 shows the dependence of solenoidal field integrals on the electron energy. The spin rotator will be based on superconducting solenoid magnets with magnetic fields in the 7 T to 10 T range. High-temperature superconducting technology might be considered to produce even higher fields.

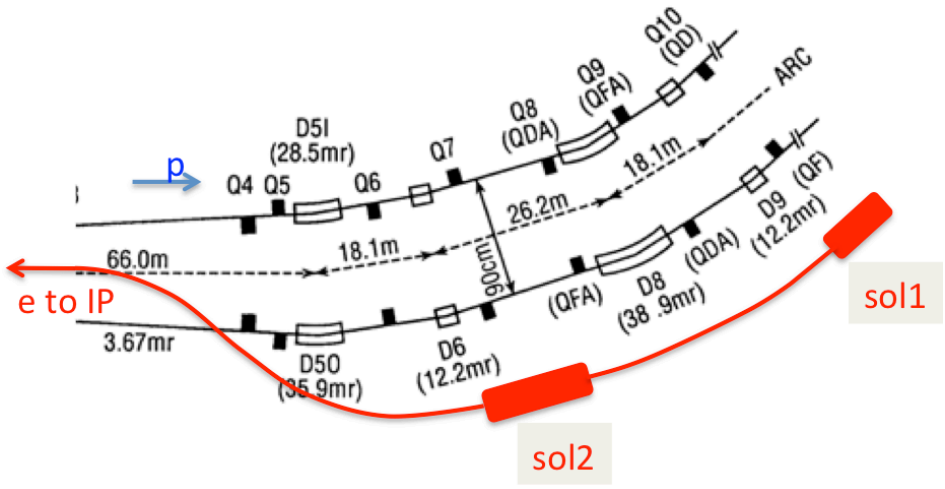

Figure I-35: Layout of the electron spin rotators.

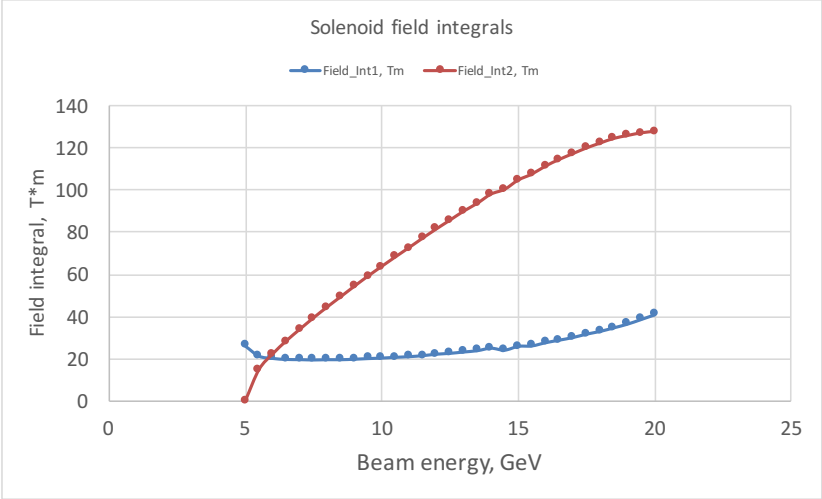

Figure I-36: Solenoidal field integral of 1st and 2nd rotators.

I.3 Hadron Beam Upgrades

I.3.1 Beam Pipe Heating and Copper Coating

High wall resistivity in accelerators can result in unacceptable levels of resistive heating or in resistive wall induced beam instabilities [22]. This is a concern for the Relativistic Heavy Ion Collider (RHIC) machine, as its vacuum chamber in the cold arcs is made from relatively high resistivity 316LN stainless steel. This effect can be greatly reduced by coating the accelerator vacuum chamber with oxygen-free high conductivity copper (OFHC), which has conductivity that is three orders [23,24] of magnitude larger than 316LN stainless steel at 4 K. But, any coating has to prevent electron cloud formation that has been observed in many accelerators, including RHIC

[25,26,27], which can act to limit machine performance through dynamical beam instabilities and/or associated vacuum pressure degradation.

Formation of electron clouds is a result of electrons bouncing back and forth between surfaces, with acceleration through the beam, which can cause emission of secondary electrons resulting in electron multipacting. Accelerator vacuum chambers and beam pipe surfaces with high enough secondary electron yield (SEY), whose typically maximum value SEY max > 1.3, facilitate electron multiplication. Original plans were to add a second coating layer on top of OFHC of TiN or amorphous carbon (a-C) to reduce secondary electron yields [28,29]; but, later results [30] indicated that a-C has lower SEY max than TiN in coated accelerator tubing. Nevertheless, new experimental SEY measurements indicated that there was no need to pursue a-C coating either; since well-scrubbed bare copper can have its SEY max reduced [31] close to 1 (SEY max < 1.3 is needed to eliminate electron cloud problems). In essence copper coating can resolve the resistivity issue, and after scrubbing can reduce SEY max below 1.3, i.e. detrimental effect of electron clouds can be marginalized.

Applying such coatings to an already constructed machine like RHIC without dismantling it is rather challenging task due to the small diameter bore (of 7.1 cm) with access points that are about 500 m apart. A device and technique were developed for *in-situ* coating of the RHIC cold bore vacuum tubes. Experiments proved that the device and technique could successfully be utilized to coat the RHIC cold bore vacuum tubes. But before embarking on the large task of coating RHIC, additional studies are needed to ensure that the expected benefits of coating the RHIC cold bore vacuum tubes with 10 μm of copper are realized. In the non-cryogenic (warm) sections, of most accelerators including RHIC, where high resistivity is not an issue, the electron cloud problem was solved by using non evaporable getters [32] (NEG).

Since the RHIC geometry is very conducive to cylindrical magnetrons due to the length to radius ratio of the RHIC beam pipe, the choice of a long cylindrical magnetron, similar to that described by A.S. Penfold in reference [33]. Ideally, that cylindrical magnetron should be made as long as possible in order to coat sections as long as possible while minimizing or eliminating any need for cathode replacements. The RHIC cold section has varying curvature (with an overall curvature of approximately 1.8 mrad per meter), which does not limit magnetron length. But, mechanical constraint to prevent any sagging does limit the magnetron cathode length to 50 cm.

A 50-cm cathode magnetron mole was developed to in-situ copper coat cold bore RHIC tubes to alleviate unacceptable ohmic heating. The magnetron has a 50 cm long copper cathode, which is shown in Figure I-37. The magnetron is mounted on a carriage with spring loaded wheels that successfully crossed bellows and adjusted for variations in vacuum tube diameter, while keeping the magnetron centered. The carriage can also be seen in Figure I-37. Some deposition experiments were performed with spring loaded wheels on both sides of the magnetron, such that a set of wheels rolls over coated areas. No indentation in or damage to coating was observed, i.e. a train like assembly option for coating 500 meter RHIC sections without any interruptions is viable.

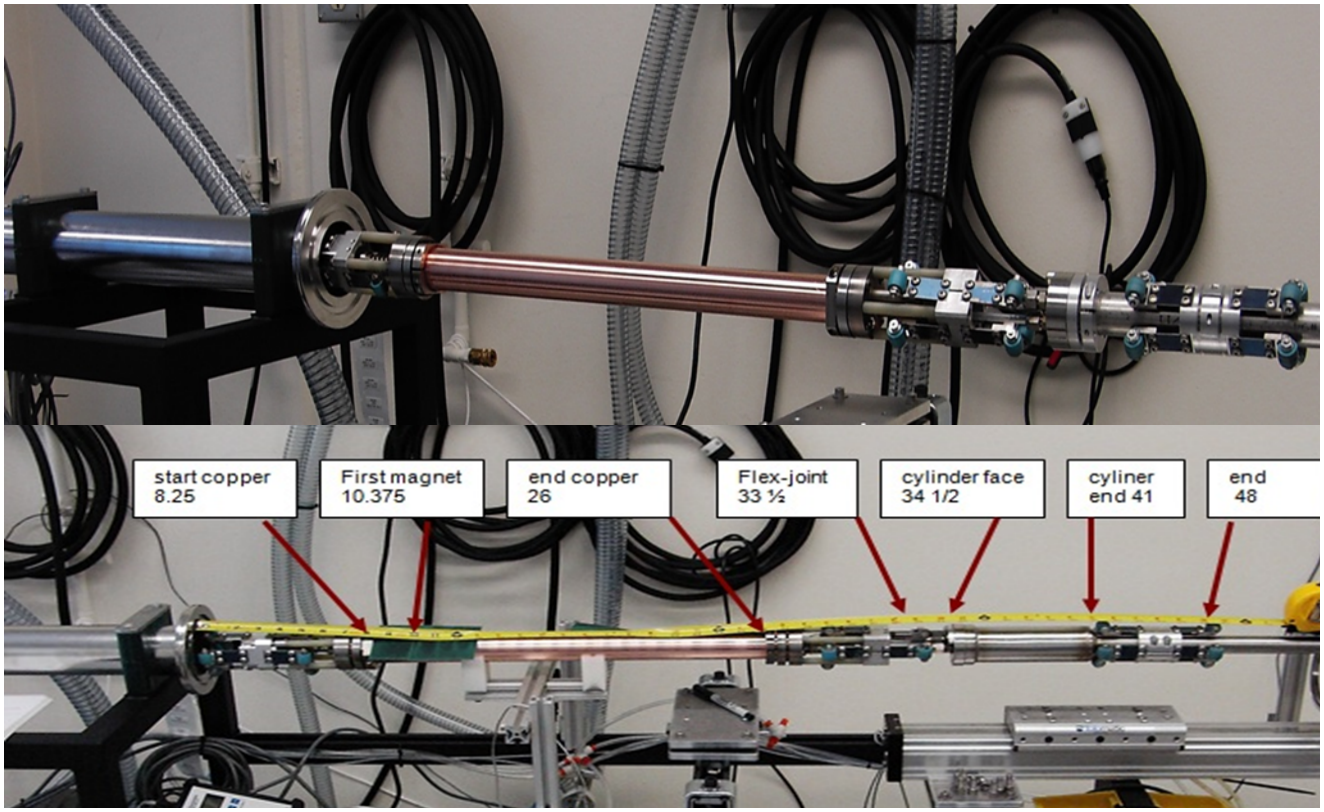

Figure I-37: Magnetron Coating Mole: Top: 50-cm long cathode magnetron, spring loaded guide wheels that crossed bellows; adjusted for diameter variations keeping magnetron centered. Bottom: the 50-cm long cathode magnetron assembly.

Problems that needed to be overcome were developing deposition procedures that result in consistently good adhesion, and maximizing copper utilization. A procedure was formulated procedure for achieving copper coating with excellent adhesion: first is application of a positive voltage (about 1 kV) to the magnetron or a separate cleaning anode and to move the discharge down the tube with a pressure of nearly 2 Torr. Second is a conventional deposition process at a pressure of about 5 mTorr.

To maximized copper utilization and minimize reloading needs, magnetron with moving magnets & thickest possible cathode is used, which reduces the target to substrate distance to less than 1.5 cm (unprecedented). Best moving magnetron magnet package moving mechanism was achieved by a miniaturized internal motor.

With the above magnetron mole and procedures, consistent coatings with excellent adhesion are achieved routinely. The optimized results yielded *adhesion strength of over 12 kg* (maximum capability pull test fixture) or at least $2.9x10^6$ N/m^2; and copper utilization reached a remarkable 85%. An assembly of a RHIC magnet tube sandwiched between two types of RHIC bellows including a shielded bellow with additional sections of RHIC tubing were connected to each bellow for a total length of about 20 meters was successfully copper coated. Routine magnetron operation has coating rate 0.0125”/sec or $3.175x10^{-4}$ meter/sec in 500 W DC operation. Therefore, it would take $1.57x10^6$ seconds or 18.22 days of magnetron sputtering operation to coat a 500 meter long section of RHIC.

The magnetron assembly was mounted on a carriage (mole) pulled by a cable assembly driven by an external motor. The cable bundle, which is enclosed in 1 inch diameter stranded SS (or braided copper), contains electric power and water cooling feeds, as well as some instrumentation wires.

Umbilical spool chamber and the cable assembly are under vacuum. Scaling the umbilical motorized spool drive system to a 500 m cable bundle yields a system that is 3 meters or less in any dimension (plenty room in the RHIC tunnel). Pull cable will be ¼" diameter stranded SS, is typically used in aircraft for flexible linkage with the various airfoil surfaces; very strong (20K tensile) with low elongation.

Room temperature RF resistivity measurements were performed on 32 cm long RHIC stainless steel tubes coated with 2 μm, 5 μm, and 10 μm, thick OFHC with a folded quarter wave resonator structure. Those measurements indicated that for the later 2 coatings conductivity was about *84% of pure copper. Since joints and connectors reduce the experimentally measured Q, the conductivity value of coatings may be even closer to pure solid copper.* Computations indicate that 10 μm of copper should be acceptable for even the most extreme future scenarios.

Nevertheless, the deposition technique must be modified, since at low temperatures, electrical conductivity is strongly affected by lattice imperfections and impurities. Room temperature conductivity is dominated by conduction band electrons, while at cryogenic temperatures, lattice defects and impurities scatter-off electrons causing large conductivity reduction. Ion assisted deposition (IAD) has been known to produce deposition with far superior qualities by establishing gradual transition between the substrate and deposited material resulting in denser more adherent film eliminating microstructure and increasing packing densities of optical coatings by an order magnitude. However, IAD requires simultaneous use of an evaporator and an ion beam source (too large for use in RHIC).

Future plans are to modify current deposition system to incorporate IAD; based on recent breakthrough IAD can be done with *End-Hall ion source*, which can be *miniaturized*; adapted for the mole. To minimize impurities, many of the deposition source components will be fabricated from the metal to be deposited. More details can be found in [34,35].

I.3.2 Proton Polarization

The parameters for eRHIC proton beam is 70% polarization with 3×10^{11}/bunch and 0.2 πmm-mrad normalized rms emittance. This emittance is at store and is expected to be cooled down by electron cooling. On the ramp, the emittance will be larger as delivered by AGS. The resonance strength associated with the larger emittance will be stronger. This section describes how the 70% polarization can be achieved based on current status of RHIC polarized proton operation and possible snake configuration changes.

Current status

The current proton acceleration chain is shown in Figure I-38. High intensity and high polarization H− is produced from the polarized proton source. The H− beam polarization is measured at the end of 200 MeV linac as 80-82%. The beam is then strip-injected into AGS Booster. The Booster vertical tune is set high so that $0 + \nu_y$ intrinsic resonance is avoided. Two imperfection resonances are corrected by orbit harmonic correction. In the AGS, two partial Siberian snakes separated by 1/3 of the ring are used to overcome the imperfection and vertical intrinsic resonances [36]. The vertical tune on the energy ramp is mostly above 8.98, so that it is in the spin tune gap and away from the high order snake resonances. To avoid the horizontal intrinsic resonances driven by the partial snakes, a pair of pulsed quadrupoles are employed to jump cross the many weak horizontal intrinsic resonances on the ramp [37]. Two full Siberian snakes are used in each of the two RHIC rings to

maintain polarization [38]. The betatron tune, coupling and orbit feedback on the energy ramp are also crucial for polarization preservation.

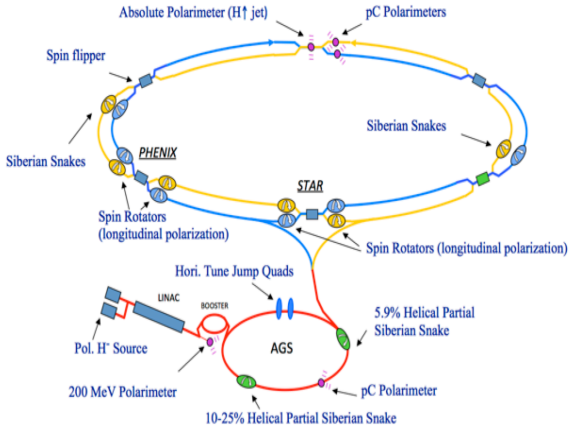

Figure I-38: Layout of current RHIC complex for polarized protons.

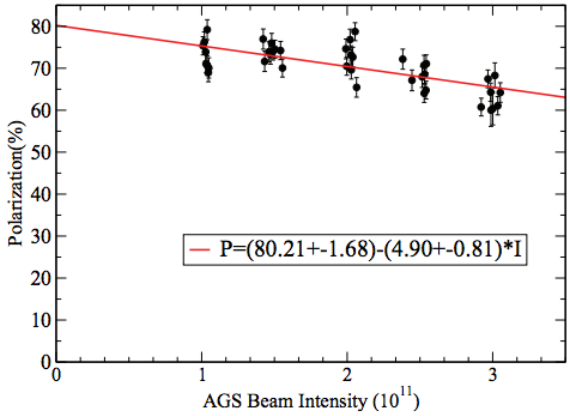

Figure I-39: AGS polarization at extraction as function of bunch intensity. The polarized proton source can deliver intensity of 9×10^{11} at the Booster input. Booster scraping (both horizontal and vertical) is used to reduce the beam emittance for AGS injection. The intensity is changed by varying the Booster scraping level.

The polarization measured at the AGS extraction is shown in Figure I-39 as function of beam intensity. The intensity was reduced by Booster scraping. The polarization dependence on intensity is really dependence on emittance. As higher intensity is always associated with larger emittance, and consequently stronger depolarizing resonance resonance strength, lower polarization is expected for higher intensity. As shown in Figure I-39, the polarization at 3×10^{11} is about 65%. The AGS Ionization Profile Monitor (IPM) can measure beam emittance but the measured beam size is affected by space charge force. To mitigate the effect, the RF is turned off at flattop. The emittance reported by IPM with RF off is plotted in Figure I-40. Since there is possible emittance growth in the Booster and mismatch in the transfer line, the projected emittance with zero intensity is not zero.

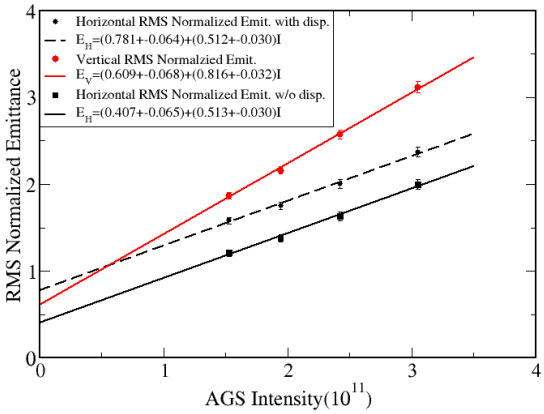

Figure I-40: AGS emittance measured by IPM vs. intensity at the AGS extraction. The dispersion is not zero at the location of IPM. The horizontal emittance without dispersion contribution is derived based on measured dp/p and model dispersion.

At 3×10^{11}, rms normalized vertical emittance is about 3π, rms normalized horizontal emittance is about 1.8π. These are emittances we are going to dealt with on the energy ramp. As the running experience shows, the polarization transmission efficiency up to 100 GeV in RHIC is close to 100% but about 85% for 250 GeV and 1.8×10^{11} bunch intensity, due to stronger intrinsic resonances. The intrinsic resonance strength can be calculated from DEPOL [39]. The results are shown in Fig. 4.

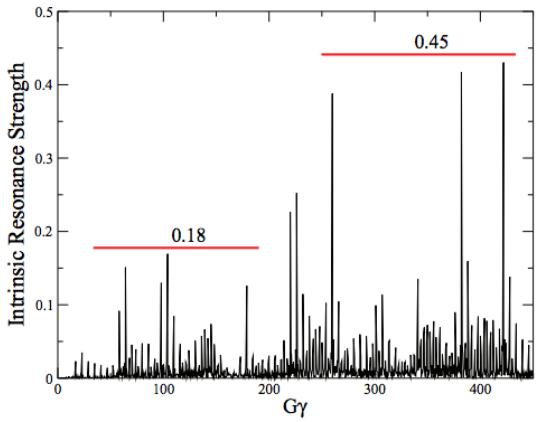

Figure I-41: The intrinsic resonance strength of RHIC lattice for a particle on a 10π normalized emittance invariant. Below 100 GeV, the resonance strength is less than 0.18. To accelerate proton beam to 250 GeV, the stronger resonance strength of 0.45 has to be overcome.

As Figure I-41 shows, the highest resonance strength for particle on 10π normalized emittance invariant is about 0.18 below 100 GeV and is about 0.45 beyond 100 GeV. The resonance strength threshold for full polarization preservation with two snakes may lie between 0.18 and 0.45. In the electron-ion collider stage, only one hadron ring is needed. In this case, the spin manipulating devices in both hadron rings can be used in one ring. Six snakes can be made from combining four existing snakes into one hadron ring, and reconstructing additional two snakes from spin rotators. In this case, six snakes will be available in the hadron ring. As a rule of thumb, the resonance strength threshold should increase by the same factor as number of snakes. Since the real resonance threshold is unknown, simulations are needed to see if polarization can be preserved for six-snake case.

Spin simulations

To estimate the polarization transmission efficiency on the ramp, spin tracking was done for one of three strongest resonances 411 – ν_y with ZGOUBI code [40]. The tracking were done for 8 particles on $\sigma = 2.5\pi$ vertical emittance ellipse. To speed up the tracking, the acceleration is 7 times of normal acceleration rate. It should be noted that with snake inserted, polarization loss is not sensitive to resonance crossing speed. Only vertical betatron motion is included in the simulation. For comparison purpose, the simulations are also done for 2-snake case. The results are shown in Figure I-42. As shown inFigure I-42, the 2-snake is not enough to preserve polarization for beam particles outside normalized rms emittance 2.5π.

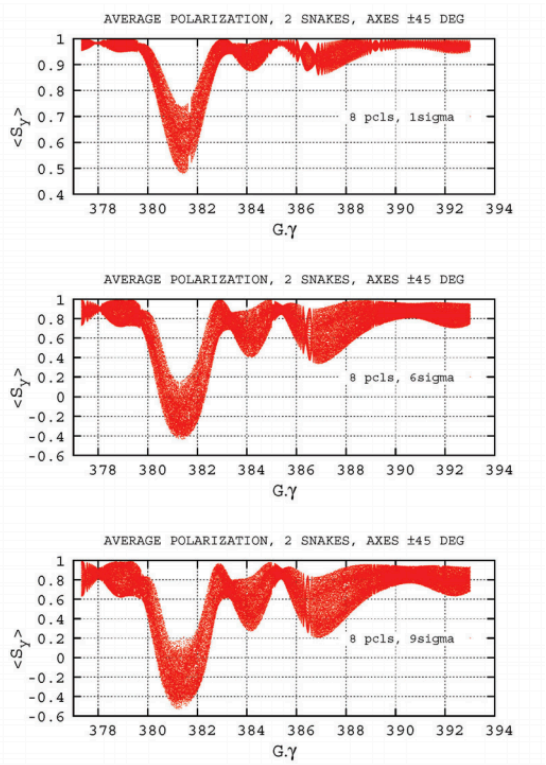

Figure I-42: Spin simulation results for 2 snakes, snake axis as ±45 degrees. From top to bottom, the vertical invariant is ε_y = 1, 6, 9σ, with σ = 2.5πmm.mrad normalized emittance. Each plot shows the average vertical projection of the spin, computed from the tracking of 8 particles evenly distributed on the invariant. The horizontal invariant is negligible. The polarization is preserved for the 2.5πmm.mrad case, but not the realistic large emittance case.

For multiple snakes scenario, the snake arrangement has to satisfy the condition for energy independent spin tune, namely

$$\sum_{k=1,3,5} \theta_{k,k+1} = \pi, \quad \sum_{k=2,4,6} \theta_{k,k+1} = \pi.$$

The axis angles are at $\phi = \pm 45^\circ$ from longitudinal axis in the local Serret-Frenet frame, so ensuring respectively Qs = 3/2, following

$$Q_s = \frac{1}{\pi} \left| \sum_{k=1}^{N_s=6} (-)^k \phi_k \right|.$$

Not all snake arrangements satisfying above conditions will preserve polarization. However, a simple arrangement with the six snakes equally spaced by 2π/6 can preserve polarization. The

simulations with ZGOUBI are also done for 6-snake configuration and the results are shown in Figure I-43. It shows that the polarization is preserved for the small and large emittance cases.

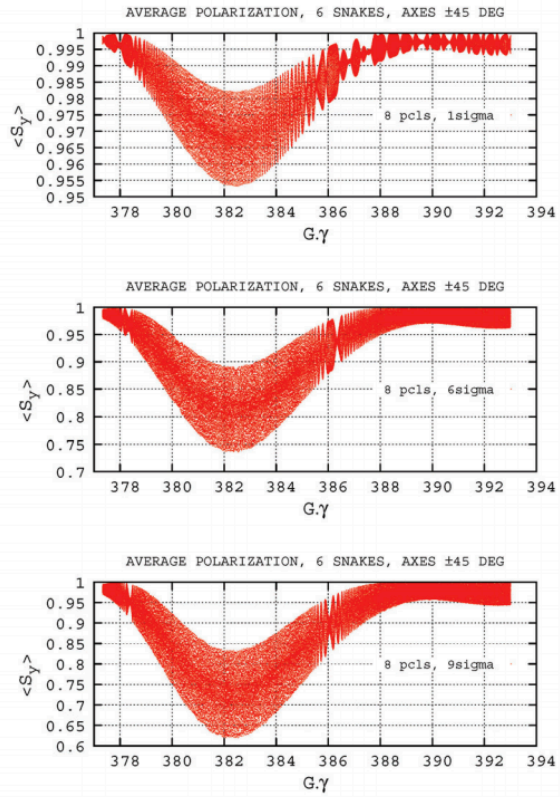

Figure I-43: The simulation results for 6 snakes, snake axis as ±45 degrees. From top to bottom, the vertical invariant is ε_y = 1, 6, 9σ, with σ = 2.5πmm.mrad normalized emittance. Each plot shows the average vertical projection of the spin, computed from the tracking of 8 particles evenly distributed on the invariant. The horizontal invariant is negligible. The polarization is preserved for all cases.

Summary

In run13, proton beam reached 60% polarization for experiments at 250 GeV for collisions with 1.8 × 10^{11} bunch intensity [41]. Currently, AGS can deliver 65% polarization with 3×10^{11}. The additional gain in AGS polarization will come from vertical emittance preservation in AGS, so that the resonance strength can be reduced. A new electron collecting IPM has been added to measure emittance in the AGS, in particular to measure the injection turn-by-turn emittance for possible emittance growth due to injection mismatch. At 250 GeV, with 6-snake configuration, the polarization transmission efficiency is close to 100% in RHIC. Spin simulations with multi-particles and 6-D distribution for real acceleration rate will follow. The optics in RHIC is also important to control possible emittance growth at injection and on the ramp. All of these then can lead to smaller emittance and higher polarization required by eRHIC. The additional emittance reduction will be done by electron cooling.

I.4 Interaction Region Design

I.4.1 Interaction Region Overview

The main features of the eRHIC interaction region are:

- Low β*: 26/13 cm (and 5/5 cm x/y in the Ultimate design)
- 14 mrad total horizontal crossing angle in a crab-crossing scheme.
- First magnet (a hadron quadrupole) is located at 4.5 m from the collision point and is outside the experimental detector.
- The hadron IR quadrupoles and dipoles are large aperture superconducting magnets,
- The hadron magnets provide free-field regions for the electrons to pass close by.
- Prevent synchrotron radiation generation with only gentle electron bending nearby the detector to avoid creation of experimental background.
- Detection of forward neutral and charged particles is accomplished by dedicated detector components placed close to the outgoing hadron beam.

The experimental requirements for the detection of forward propagating products of the collisions significantly impact the IR magnet designs. In the outgoing hadron beam direction, the IR magnets must provide sufficient aperture to pass the forward neutrons and forward scattered protons with a typical angular spread on the scale of ±5 mrad. At the same time Roman Pots integrated into the IR design should be able to register protons with transverse momentum as small as 200 MeV/c. In the outgoing electron beam direction the electron magnet apertures must accommodate scattered electrons with small scattering angles (25-35 mrad) for experimental tagging while passing photons generated at the IP on to a luminosity monitor. The very challenging IR geometry of the forward side is shown in Figure I-44.

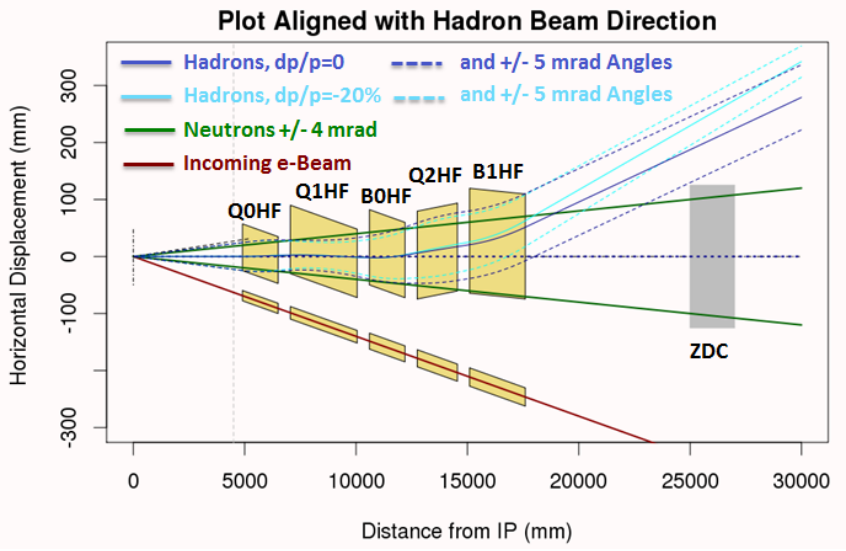

Figure I-44: eRHIC forward side interaction region layout (the view from above). The separate horizontal apertures for both electrons and hadrons are shaded yellow in this figure.

The main challenge here is to pass a full 4 mrad neutron cone through these IR forward magnet apertures to a Zero Degree Calorimeter (ZDC) while magnetically separating the neutrons from other ±5 mrad forward-going charged particles (that are measured in other detector elements) and the circulating hadron beam. The circulating hadron beam needs strong focusing for the IR optics and strong deflection fields to cleanly provide the degree of charged beam separation required by the experiment. This combination of large magnet apertures and strong fields could easily lead to intolerable external fields at the incoming electron beam path if no special measures were taken.

The Sweet Spot scheme adopted for passing the electrons through a very low field area between the coils of hadron IR magnet is illustrated in Figure I-45. The extended low field "sweet spot" is made by combining the fields produced by main, middle and outer coil structures and passive shielding. The particular coil geometry shown is effective for passing the electrons just outside an otherwise high field region near the main hadron quadrupole coil because the field contributions from the various coils add constructively inside the hadron aperture but largely cancel one another in the sweet spot region [42].

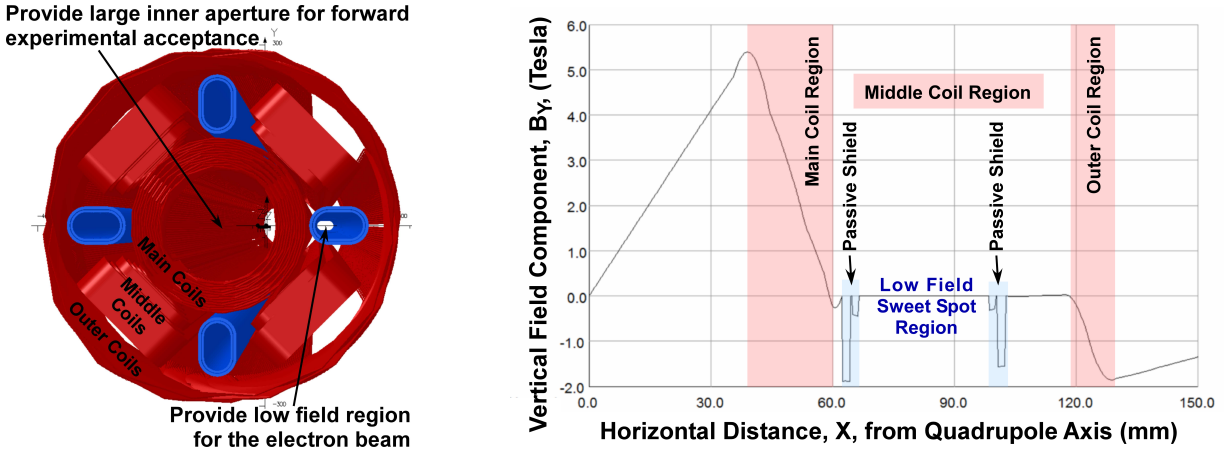

Figure I-45: Left plot: the 3d coil profile with the various coil windings and apertures identified; Right plot: the field profile generated at the middle of the magnet.

On the rear side of the IR (opposite side where the electron beam leaves the detector) the required hadron apertures are much smaller and the rear hadron superconducting magnet coils are accordingly much more compact than those of the forward side. Thus it is possible to ensure adequate external field shielding for the rear side electrons by providing simple cutout regions for the electrons to pass through the hadron magnetic yokes.

I.4.2 Hadron IR Lattice

The hadron beamline lattice functions for the Low Risk design are plotted in Figure I-46. The vertical beta-function reaches a maximum value of 1050 m in an IR defocusing quad. The horizontal beta-function has been flattened through the crab-cavity area.

The IR design has been developed to satisfy goals of the Ultimate design, to avoid costly IR upgrade when upgrading the eRHIC luminosity. Reaching β^* = 5 cm required for the high design luminosity in the Ultimate design is done in two steps. First, the interaction region quadrupoles are designed to provide a strong focusing which allows to achieve β^* as low as 10 cm. Then, the

squeeze from 10 cm to 5 cm is realized by introducing betatron waves in both planes, using the Achromatic Telescope Squeezing technique [43]. The eRHIC hadron lattice has a phase difference of 90° per cell in the arcs. The betatron wave is created by changing the quadrupole gradients (ΔG= 7% with respect to the regular arc quadruple gradients) in two quadrupole pairs at the beginning of the arc before the IP.

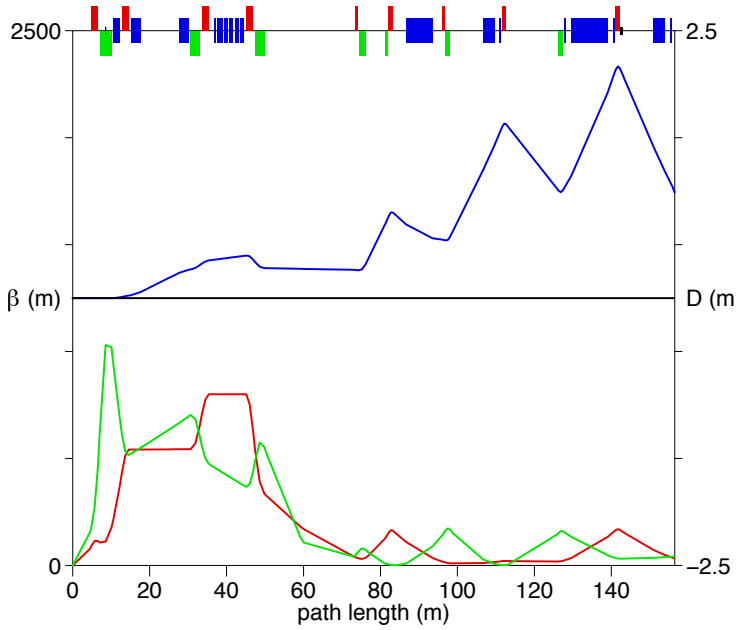

Figure I-46: Hadron lattice functions of eRHIC interaction region, corresponding to $\beta_x^*=26$ *cm*, $\beta_y^*=13$ *cm*.
Red curve - horizontal β, green curve – vertical β, blue curve –dispersion function.

24 families of sextupoles in the 90° degree lattice are able to correct the first and higher orders of chromaticities in the eRHIC lattice. The sextupole strength can be optimized also to minimize the lower order resonance driving terms. The resulting dynamic aperture (for the IR lattice variant with β_{max} *~2200*) obtained in the presence of the machine errors as well as beam-beam interactions is shown in Figure I-47. Machine errors include 0.2% quadrupole and sextupole field errors and 100 microns magnet misalignments. At the momentum spread of the cooled hadron beam of $\sim 2\cdot 10^{-4}$, the sufficient dynamic aperture of 10σ has been demonstrated. Further improvement may be expected from careful choice of the machine working point.

Similar dynamic aperture studies will be repeated for the Low Risk design parameters, although those parameters are less demanding than in the Ultimate design.

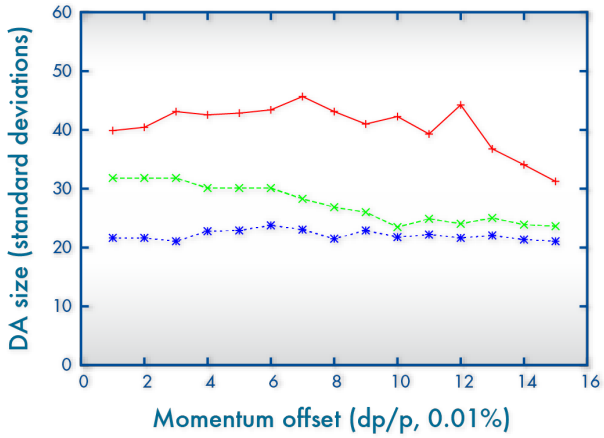

Figure I-47: A plot of the optimized off-momentum dynamic aperture for eRHIC. The top curve (red, +) is the bare lattice, the middle curve (green, x) is with a beam-beam parameter of 0.015, and the bottom curve (blue, *) is with beam-beam and gradient errors.

I.4.3 Electron Beamline

The beam is extracted into the highest energy beamline in the spreader area. This beam line runs around all RHIC tunnel circumference. In the interaction region area the highest energy beamline brings the electrons to the experimental detector along its axis and focuses the beam to required small at the collision point. The beamlines upstream and downstream of the detector have a similar magnet and lattice structure.

The Figure I-47 shows as an example the electron optics in the interaction region area, developed for a previous design of eRHIC. But similar approach we are going to implement for the Low Risk design electron lattice.

The bending used in ~60m area from the interaction point, which puts the electron beam exactly on the detector axis, is very gentle. The beamline in this area contains the bending magnets with the field from 95 to 14 Gs at 18 GeV beam energy. Using the 14 Gs dipole magnets for the final bending produces a very low intensity soft synchrotron radiation, which does not create problems at the detector. The final focusing triplet, provide required beta-function at the collision point.

Since there are no strong bending magnets within 60 m from eRHIC detector, there are no strong synchrotron radiation sources near the experimental detector. The forward radiation coming from the upstream hard bend is completely masked and no hard radiation passes through the detector. Only soft bending is present in the vicinity of the detector. The forward radiation from the upstream soft bend passes through the detector but cannot penetrate through the beam pipe. The secondary backward radiation induced by the forward radiation generated in downstream bends can be mostly masked from entering the detector area.

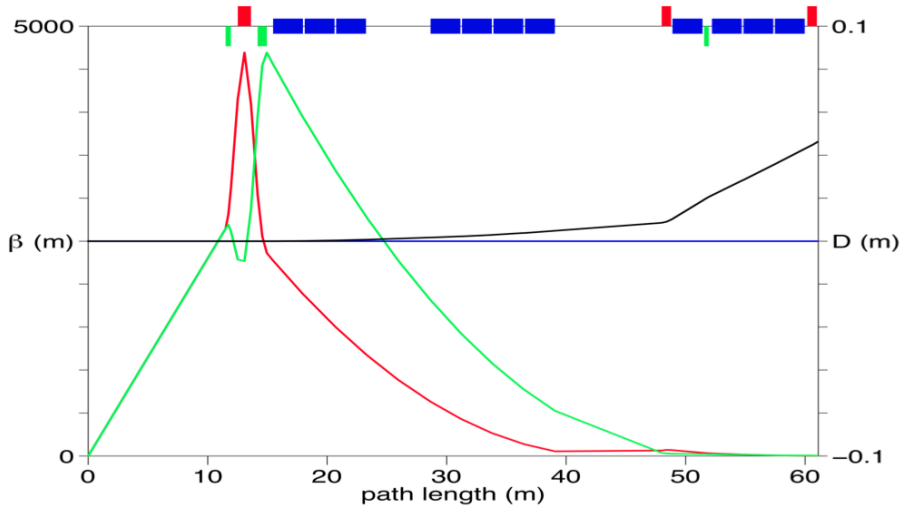

Figure I-48: The horizontal (red) and vertical (green) beta-functions, and the horizontal (blue) and vertical (black) dispersion functions of the electron IR beamline for the case β*=5 cm. The collision point is located at 0 of the horizontal axis. is shown.

I.4.4 Crab-Crossing

Since the interaction region employs 14 mrad crossing angle between electron and hadron beams, the crab-crossing scheme is required to avoid more than an order of magnitude of luminosity loss. Crab cavity is required to establish crab crossing scheme in eRHIC. Ideally it should provide transverse kick which is linearly proportional to its relative longitudinal position within the bunch and form a tilting angle of half of the crossing angle on both colliding beams to compensate crossing angle. As a result, the two beam will collide equivalently to the head-on collision. The crab cavities are placed on both sides of the interaction region area to ensure that the beam rotation does not propagate to the outside of the interaction region.

If the bunch length is comparable with the wavelength of the crab cavity, the sinusoidal form of the crab-cavity voltage leads to the transverse deviation of particle at the head and tail of the bunch from the perfect linear x-s correlation. This nonlinearity not only leads to the luminosity loss, but also induces transverse kicks to the both beams which depend on the longitudinal position. The longitudinal dependent kicks together with the beam-beam interaction may reduce the dynamic aperture of the ion beam as well as induce emittance growth.

Before detailed simulation with the crab cavity, we use luminosity degradation parameter to quantitate the effect of the nonlinear kick from the crab cavity, and determine the frequency of the crab cavities for both Nominal and Ultimate design.

The luminosity degradation parameter $H = L_{crab\text{-}crossing} / L_{head\text{-}on}$ characterizes the integral effect of the nonlinear crab cavity. An ideal crab cavity will recover the luminosity from the crossing angle and make this parameter 1. We set the criteria of the degradation to be 0.95, which is similar to the value of the LHC High Luminosity upgrade. The effect of the beam-dynamics requires further simulation.

We propose to use two frequencies, a fundamental frequency 140.7 MHz and its 3rd harmonic frequency 422.2MHz. The voltage ratio of the harmonic cavity is determined by minimizing the luminosity degradation factor. We found that the optimum ratio is 0.17. The detailed parameter is listed in Table I-12. The 422.2 MHz cavity will also serve as the crab cavity of the electron beam. The voltage of the fundamental and the high harmonic cavities are:

$$V_1 = \frac{cE_b\theta_c}{e\omega_1 R_{12}}(1+\alpha); V_3 = -\frac{cE_b\theta_c\alpha}{e\omega_3 R_{12}}$$

where E_b is the beam energy, θ_c is the half crossing angle, and R_{12} is the component of the transverse map from crab cavity to IP.

eRHIC crab cavity design will be based on the same geometry as the cavity for the LHC high-lumi upgrade, with necessary scaling and optimizations accordingly. The LHC Accelerator Research Program in the Collider Accelerator Department of Brookhaven National Lab has delivered a successful compact crab cavity design for the Hi-Lumi upgrade of LHC, shown in the left of Figure I-49. This 400 MHz crab cavity is based on a double quarter wave (DQW) geometry with push-pull tuning system, three higher order mode couplers, and a 50 kW fundamental power coupler, as shown in the right of Figure I-49. The Proof of Principle DQW crab cavity has reached 4.6 MV in deflecting voltage at 2 K cold test. The compactness of the DQW crab cavity ensures the size in all three dimensions to keep within an economical value even at low frequencies, such as the 140.7 MHz for the fundamental crab cavity for ion/proton. The high frequency cavities for electron crabbing and 3rd harmonic correction for ion/proton should be very close to the LHC cavity design, which maximized the reuse of the experience gained previously.

Table I-12: Crab cavity parameters.

Parameters	Low Risk Design	
	Electron	Ion (p)
Crossing angle (Full, mrad)	14	
Beam energy (GeV)	18	275
Horizontal beta function at IP (β^*, cm)	26	26
Transverse beam size at IP (μm)	15.3	15.3
Bunch length (cm)	0.3	16
Piwinski angle (rad)	0.7	37.6
Beta function at crab cavity	~100	~800
Frequency of fundamental crab cavity (MHz)	422.2	140.7
Voltage of fundamental crab cavity (MV)	3	~53
Frequency of 3rd harmonic crab cavity (MHz)	N/A	422.2
Voltage of 3rd harmonic crab cavity (MV)	N/A	~-2.5

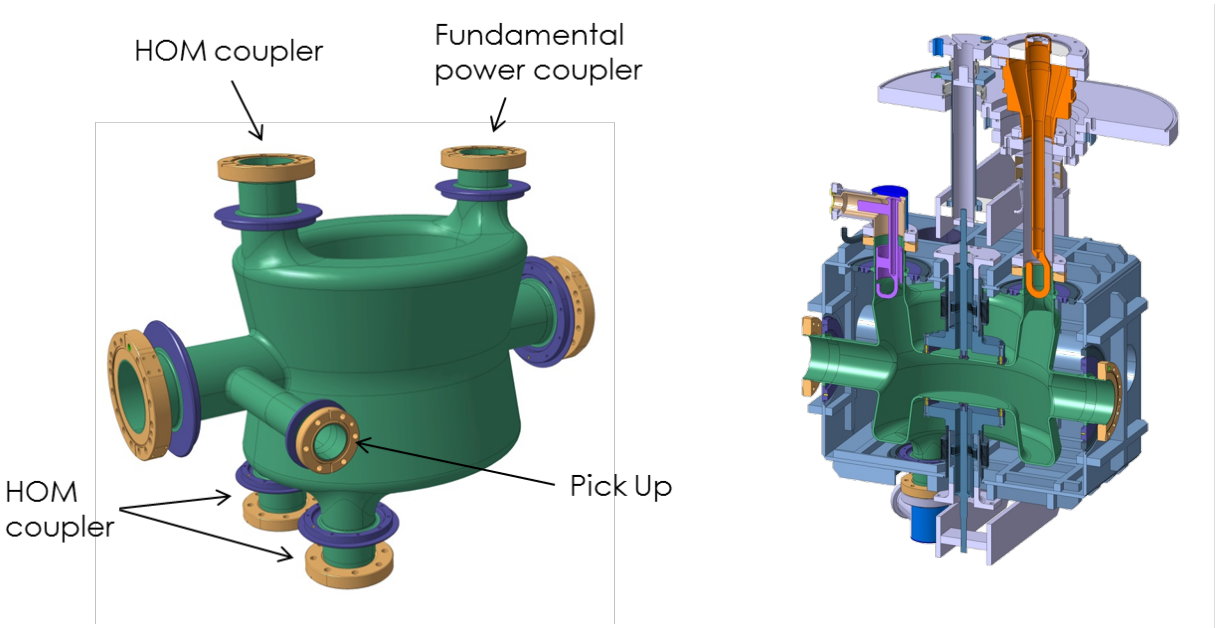

Figure I-49: Left: DQW crab cavity for Hi-Lumi LHC; right: Cross-section view of the DQW crab cavity in helium vessel with HOM coupler (purple), 50kW FPC (orange), and tuner.

I.5 Pathway for Luminosity Upgrade.

The ERL-ring approach strongly benefits from the hadron cooling since at fixed beam angular spreads (σ_x', σ_y') at the interaction point the luminosity scales as an inverse square of transverse emittance ε:

$$L \sim \frac{I_e N_p \sigma_x' \sigma_y'}{\varepsilon^2}$$

where I_e is the electron beam current and N_p is the number of protons per bunch. A successful high-energy proton cooling R&D will open a straightforward path to the luminosity upgrade by reducing transverse emittance. To maximize luminosity a longitudinal cooling also has to be applied in order to follow reduced β* with a shorter bunch length.

In order to reach the 10^{34} cm^{-2} s^{-1} luminosity level (the Ultimate design of eRHIC) the cooling of 250-275 GeV protons must be strong enough to counteract IBS growth rate of 5-10 min. Such cooling rates are expected from advanced cooling techniques, like the coherent electron cooling [44] and the micro bunching electron cooling [45]. R&D efforts are underway for these advanced cooling techniques, including the proof of principle experiment at RHIC for coherent electron cooling [46].

The interaction region described in the section I.4 has been designed to be suitable for β* as low as 5cm. Thus, no IR upgrade is needed to reach the Ultimate design parameters. Table I-13 lists parameters of the Low Risk and Ultimate designs. In the Ultimate design the proton beam is cooled down to the limit defined by proton beam-beam and space charge parameters.

Table I-13: Beam parameters for highest luminosity of e-p collisions for the Low Risk design, and for the Ultimate design.

	Low Risk ERL-Ring Design		Ultimate ERL-Ring Design	
	e	p	e	p
Energy [GeV]	13	275	8.3	250
CM energy [GeV]	105		91	
Bunch frequency [MHz]	9.4		9.4	
Bunch intensity [10^{10}]	3.3	30	3.3	30
Beam current [mA]	50	415	50	415
rms norm.emittance h/v[um]	64/64	1/1	16.5/16.5	0.27/0.27
rms emittance h/v [nm]	2.5/2.5	3.4/3.4	1.0/1.0	1.0/1.0
beta*, h/v [cm]	35/17.5	26/13	7/7	7/7
IP rms beam size h/v [um]	30/21		8.4/8.4	
IP rms ang. .spread h/v [urad]	85/120	115/163	120/120	120/120
max beam-beam parameter	1.0	0.004	4.1	0.015
e-beam disruption parameter	6		36	
max space charge parameter	9e-5	0.004	8.6e-4	0.058
rms bunch length [cm]	0.3	16	0.3	5
Polarization [%]	80	70	80	70
Peak luminosity [$10^{33}cm^{-2}s^{-1}$]	1.2		14.4	

I.6 Risk Assessment and Mitigation

Following are leading risks of the ERL-Ring design. Planned mitigation of these risks is described.

1. The high current polarized electron source presents the biggest remaining design risk. Required 50 mA beam current has not been demonstrated yet from a single polarized electron gun. Hence, the design adopts a multi-gun approach where the high current is obtained by combining beam currents produced by eight individual guns. Based on results from JLab [47] where a beam current of 4mA was demonstrated with several hours cathode lifetime, it is considered feasible to achieve a beam current of 6.25 mA from each of eight guns with at least several hours cathode lifetime. The combiner scheme uses RF field copper plate deflectors, at maximum frequency 4.7 MHz. Dealing with high bunch charge (5 nC) presents an additional complication, although the bunch charge of 7 nC from a polarized gun was demonstrated in 2 ns pulses at SLAC [48]. The study plan includes simulations of high charge beam transport through the combining system as well as experimental studies of high bunch charge effects and cathode lifetime dependencies at the Gatling gun prototype and the cathode deposition facility. During eRHIC operation an automated system will be able to make cathode re-cesiation in between stores, when needed, to restore the cathode quantum efficiency.
2. Two major design risks of high current recirculating machine: the multi-pass beam-breakup instability (MBBU) and the beam loss control. Following the knowledge gained in past and present re-circulating accelerators (such as CEBAF, JLab ERL, BINP ERL and others) the design study is going to address these risks. It is well understood that the instability threshold of MBBU can be maximized by minimizing cavity HOM impedances and by incorporating

machine lattice tools like betatron phase adjuster, betatron coupling and large chromaticity. Trustworthy simulation codes exist to accurately establish the instability threshold. In order to control beam losses all possible beam halo sources must be explored. The size of the beam halo size is the major factor for the choice of the apertures of the magnets in the re-circulating loops. The application of a collimation system (especially, to address the halo produced by the injector) will be considered. Adequate beam loss diagnostic is also required.

3. In order to preserve the luminosity in the IR with the crossing angle a crab-crossing scheme is adopted. The crab-crossing was used to increase the luminosity of electron-positron collider KEKB [49]. The crab-crossing technology has not yet been used in past hadron colliders, which presents a certain risk for eRHIC. However, the crab-crossing is planned as a part of high luminosity upgrade of proton-proton collider LHC [50]. For the crab-crossing in eRHIC the choice of crab-cavity parameters as well as the design of SRF crab-cavities are strongly based on developments done in the course of the LHC high luminosity upgrade. A planned beam test of crab-cavity prototypes in CERN will be also of great interest for the eRHIC design. Dedicated beam-beam simulation codes including crab-crossing will be used to study related effects.
4. The Low Risk design aims to achieve required e-p luminosities without any cooling. Smallest possible emittances must be produced from the injectors and then preserved during the RHIC energy ramp. Planned studies for achieving minimal emittance are going to address possible effects leading to the emittance growth at the RHIC injection and on the ramp (injection kicker timing, transverse noise, IBS, electron cloud, …) as well as further optimization of scraping technology at the injectors. Longitudinal bunch merging in injectors to get a higher bunch intensity after the scraping is also being considered.
5. Beam-beam effects in the linac-ring colliding scheme have several unique features distinguishing them from standard beam-beam effects of ring-ring colliders. Since no linac-ring collider existed distinguished features of linac-ring beam-beam interaction must be thoroughly studied with simulation codes. Considerable amount of such studies has been done in recent years for all possible harmful effects: the disruption and mismatch effect on the electron beam, the kink instability and the noise heating of the ion beam, and possible countermeasures have been developed (like, a feedback against the kink instability). This design study will continue evaluation of beam-beam interaction with simulation codes.

Bibliography:

[1] D. Schultz, R. Alley, H. Aoyagi, J. Clendenin, J. Frisch, C. Garden, E. Hoyt, R. Kirby, L. Klaisner, A. Kulikov, G. Mulhollan, C. Prescott, P. Saez, H. Tang, J. Turner, M. Woods, D. Yeremian, and M. Zolotorev, Nucl. Instruments Methods Phys. Res. Sect. A Accel. Spectrometers, Detect. Assoc. Equip. **340**, 127 (1994).

[2] C. L. Garden, E. W. Hoyt, D. C. Schultz, and H. Tang, in *Proc. Int. Conf. Part. Accel.* (IEEE, 1993), pp. 3039–3041.

[3] M. BastaniNejad, M. Poelker, J. L. McCarter, J. Hansknecht, K. E. L. Surles-Law, J. M. Grames, M. L. Stutzman, J. Clark, R. Suleiman, and P. A. Adderley, Conf.Proc. **C110328**, 1501 (2011).

[4] J. Grames, R. Suleiman, P. A. Adderley, J. Clark, J. Hansknecht, D. Machie, M. Poelker, and M. L. Stutzman, Phys. Rev. Spec. Top. - Accel. Beams **14**, 43501 (2011).

[5] T. Nishitani, T. Nakanishi, M. Yamamoto, S. Okumi, F. Furuta, M. Miyamoto, M. Kuwahara, N. Yamamoto, K. Naniwa, O. Watanabe, Y. Takeda, H. Kobayakawa, Y. Takashima, H. Horinaka, T. Matsuyama, K. Togawa, T. Saka, M. Tawada, T. Omori, Y. Kurihara, M. Yoshioka, K. Kato, and T. Baba, J. Appl. Phys. **97**, 094907 (2005).

[6] E. J. Riehn and K. Aulenbacher, in *PSTP2011* (St. Petersburg, 2011), pp. 17–20.

[7] B. Dunham, et al., "First Test of the Cornell University ERL Injector", LINAC08, WE104, Victoria, BC, Canada, (2008).

[8] D. Trbojevic et. all, “Design Method for High Energy Accelerator without Transition Energy”, 2nd European Particle Accelerator Conference, EPAC90, Nice, 11-16 June (1990) pp. 1536.

[9] S.Y. Lee, K.Y. Ng, and D. Trbojevic, “Minimizing dispersion in flexible momentum compaction lattices”, Phys. Rev. E, **Vol. 48** (1993) pp. 3040-3048.

[10]M. Borland, "elegant: A Flexible SDDS-Compliant Code for Accelerator Simulation," Advanced Photon Source LS-287, September 2000.

[11] Y. Wang and M. Borland, "Pelegant: A Parallel Accelerator Simulation Code for Electron Generation and Tracking", Proceedings of the 12th Advanced Accelerator Concepts Workshop, AIP Conf. Proc. 877, 241 (2006).

[12] F. Meot, The ray-tracing code Zgoubi - Status, NIM A 767 (2014) 112125; F. Meot, Zgoubi users’ guide, http://www.osti.gov/scitech/biblio/1062013.

[13]F. Méot, S. Brooks, Y. Hao, Y. Jing, V. Ptitsyn, D. Trbojevic, N. Tsoupas, “eRHIC ERL modeling in Zgoubi”, BNL/C-AD Note C-A/eRHIC/49 (2016).

[14] G.H. Hoffstaetter and I.V. Bazarov, Phys. Rev. ST-AB 7, 054401, (2004).

[15] E. Pozdeyev, Phys. Rev. ST-AB 8, 054401, (2005).

[16] Y. Hao, and V. Ptitsyn, Phys. Rev. ST-AB, 13, 071003 (2010).

[17] R. Li, B.C. Yunn, V. Lebedev, J.J. Bisognano, “Analysis of Beam-beam Kink Instability in a Linac-Ring Electron-Ion Collider”, PAC’01, Chicago, IL, (2001).

[18] Y. Hao, V. N. Litvinenko, and V. Ptitsyn. Phys. Rev. ST-AB, 16, 101001 (2013).

[19] Y. Hao, M. Blaskiewicz, V. N. Litvinenko, and V. Ptitsyn., “Kink Instability Suppression With Stochastic Cooling Pickup And Kicker”, IPAC’12, New Orleans, Louisiana, USA, (2012).

[20] D.P. Barber, et al., Phys. Lett. 3434B 436 (1995).

[21] T. Zwart, et al., Proceedings of PAC, Chicago, p.3597 (2001).

[22] Covered in many textbooks, e.g. A.W. Chao, “Physics of Collective Beam Instabilities in High Energy accelerators”, John Wiley & sons Inc. N. Y. (1993).

[23] R.P. Reed and A.F. Clark, Editors “Materials at Low Temperatures” American Society of Materials (1983).

[24] N.J. Simon, E.S. Drexler, and R.P. Reed, "Properties of Copper and Copper Alloys at Low Temperatures", NIST monograph 177, Government Printing Office (1992).
[25] U. Iriso and S. Peggs, Phys. Rev. ST Accel. Beams **8**, 024403 (2005).
[26] U. Iriso and S. Peggs, Phys. Rev. ST Accel. Beams **9**, 071002 (2006).
[27] W. Fischer M. Blaskiewicz, J. M. Brennan, H. Huang, H.-C. Hseuh, V. Ptitsyn, T. Roser, P. Thieberger, D. Trbojevic, J. Wei, S. Y. Zhang, and U. Iriso, Phys. Rev. ST Accel. Beams 11, 041002 (2008).
[28] E.L. Garwin, F.K. King, R.E. Kirby, and O. Aita, J. Appl. Phys. **61**, 1145 (1987).
[29] P. Chiggiato, "*Surface treatments and coatings for the mitigation of electron clouds*", presentation to the 23rd LHC Machine Advisory Committee Meeting, 16 June 2008.
[30] C. Yin Vallgren, G. Arduini, J. Bauche, S. Calatroni, P. Chiggiato, K. Cornelis, P. Costa Pinto, B. Henrist, E. Métral, H. Neupert, and G. Rumolo, Phys. Rev. ST Accel. Beams **14**, 071001 (2011).
[31] A. Kuzucan, H. Neupert, M. Taborelli, and H. Stori, J. Vac. Sci. Technol. A **30**, 051401 (2012). Mauro Taborelli, private communication 2012; M. Furman, private communication 2012.
[32] C. Benvenuti, P. Chiggiato, F. Cicoira, and Y. L'Aminot, J. Vac. Sci. Technol. A **16**, 148 (1998).
[33] John L. Vossen and Werner Kern Editors, "Thin Film Processes" Academic Press, New York (1978).
[34] A. Hershcovitch, M. Blaskiewicz, J. M. Brennan, A. Custer, A, Dingus, M. Erickson, W. Fischer, N. Jamshidi, R. Laping, C. J. Liaw, W. Meng, H.J. Poole, R. Todd, "Plasma sputtering robotic device for in-situ thick coatings of long, small diameter vacuum tubes," Physics of Plasmas 22, 057101 (2015).
[35] A. Hershcovitch, M. Blaskiewicz, J.M. Brennan, W. Fischer, C-J Liaw, W. Meng, R. Todd. A. Custer, A. Dingus, M. Erickson, N. Jamshidi, and H. J. Poole, "Novel techniques and devices for in-situ film coatings of long, small diameter tubes or elliptical and other surface contours", J. Vac. Sci. Technol. B 33, 052601 (2015).
[36] H. Huang, et al., Phys. Rev. Lett. 99, 154801 (2007
[37] H. Huang, et al., Phys. Rev. STAB. 17, 081001 (2014).
[38] M. Bai, et al., Phys. Rev. Lett. 96, 174801 (2006).
[39] E. Courant and R. Ruth, BNL report, BNL-51270 (1980).
[40] F. Meot, et al., Proc. of IPAC12, 181 (2012).
[41] A. Zelenski, H. Huang, T. Roser, Proc. of PSTP 2013, 056 (2013).
[42] B. Parker, "Sweet Spot Designs for Interaction Region Septum Magnets", in *Proc. 7th International Particle Accelerator Conference (IPAC'16)*, Busan, Korea, May 2016, paper TUPMB042, pp. 1196-1198.
[43] S.Fartoukh, "An Acromatic Telescope Squeezing Scheme for the LHC Upgrade", IPAC'11, WEPC037, (2011).
[44] V. N. Litvinenko, Y. S. Derbenev, "Coherent electron cooling", Phys. Rev. Lett. 102:114801, (2009).
[45] D. Ratner, Physical Review Letters 111, 084802 (2013).
[46] I. Pinayev *et al*., "Present Status Of Coherent Electron Cooling Proof Of Principle Experiment", WEPPO14, COOL'13, (2013).
[47] P. Adderley, et al., "CEBAF 200 kV Inverted Electron Gun", Proceed. of PAC'11, WEODS3, New York, NY, (2011).
[48] D. Schultz, et al., "The high peak current polarized electron source of the Stanford Linear Collider", Nucl. Instrum. Methods A **340**, p.127 (1994).
[49] Y. Funakoshi, et al., "Recent progress of KEKB" , Proceed. of IPAC'10, WEOAMH02, Kyoto, Japan, (2010).

[50] G. Apollinari et al., “High-Luminosity Large Hadron Collider (HL-LHC): Preliminary Design Report”, CERN- 2015-005, (2015)